

N64-25007

NASA CR-54049

Cosmic, Inc. Report No. 68

FINAL REPORT

CHARGED COLLOID GENERATING SYSTEM
FOR ELECTRIC PROPULSION

by

D. Gignoux, H. F. Anton, and J. J. Shea

prepared for

NATIONAL AERONAUTICS AND SPACE ADMINISTRATION

12 October 1963

CONTRACT NAS3-2509

Technical Management
NASA Lewis Research Center
Cleveland, Ohio
Electric Propulsion Office
Russell D. Shattuck

COSMIC, INC.
3206 Grace Street, N. W.
Washington, D. C. 20007

NOTICE

This report was prepared as an account of Government sponsored work. Neither the United States, nor the National Aeronautics and Space Administration (NASA), nor any person acting on behalf of NASA:

- A.) Makes any warranty or representation, expressed or implied, with respect to the accuracy, completeness, or usefulness of the information contained in this report, or that the use of any information, apparatus, method, or process disclosed in this report may not infringe privately owned rights; or
- B.) Assumes any liabilities with respect to the use of, or for damages resulting from the use of any information, apparatus, method or process disclosed in this report.

As used above, "person acting on behalf of NASA" includes any employee or contractor of NASA, or employee of such contractor, to the extent that such employee or contractor of NASA, or employee of such contractor prepares, disseminates, or provides access to, any information pursuant to his employment or contract with NASA, or his employment with such contractor.

Requests for copies of this report should be referred to:

National Aeronautics and Space Administration
Office of Scientific and Technical Information
Attention: AFSS-A
Washington, D. C. 20546

TABLE OF CONTENTS

	<u>Page</u>
SUMMARY	iii
LIST OF FIGURES	iv
TABLE OF SYMBOLS	vi
1. INTRODUCTION	1
2. ANALYTICAL INVESTIGATION OF THE CHARGED COLLOID SYSTEM	5
2.1 Film Flow Inside the Nozzle	5
2.2 Qualitative Explanations of Droplet Formation	5
2.3 Limit on Droplet Size and Charge-to-Mass Ratio	6
2.4 Effect of Propellant Conductivity	6
2.5 Parametric Study of System Operation, Including Space-Charge Effects	10
2.6 Relation Between the Measured and Calculated Performance Characteristics	19
3. DESCRIPTION OF COLLOID GENERATING SYSTEM AND INSTRUMENTATION	21
3.1 Colloid Generating System	21
3.1.1 Nozzle	21
3.1.2 Nozzle Spindle and High Speed Feedthrough	21
3.1.3 Propellant Metering and Feed System	26
3.1.4 Accelerating System	31
3.1.5 High Voltage Connections	31
3.1.6 Heating System for Operation with Liquid Metals	36
3.2 Instrumentation	36
3.2.1 Voltage	36
3.2.2 Currents	36
3.2.3 Mass Flow	36
3.2.4 Thrust	39
3.2.5 Angular Velocity of the Nozzle	39

	<u>Page</u>
4. SUMMARY AND DISCUSSION OF TEST RESULTS	40
4.1 Measurements of Propellant Characteristics	40
4.2 Mechanical Tests	45
4.3 Tests with Nozzle at Ground Potential	45
4.4 Tests with Nozzle at High Voltage	48
4.5 Comparison Between Predicted and Measured System Performance	55
5. CONCLUSIONS	59
REFERENCES	60
APPENDIX - Space Charge Flow Between Parallel Planes	62
DISTRIBUTION LIST	67
ABSTRACT	70

SUMMARY

An induction-charged colloid generating system has been operated satisfactorily. The rotating speed has been varied between 1,000 and 18,000 rpm, the mass flow between 1.5×10^{-6} and 120×10^{-6} kilograms/second, and the voltage between 0 and 50,000 volts. Mass flow, beam current, voltage, and thrust have been measured with a sufficient accuracy to make possible direct measurements of the efficiency. An efficiency of 80% has been obtained in repeated experiments. The system has interesting potential application to electrostatic thrusters with low specific impulse.

LIST OF FIGURES

<u>Figure Number</u>	<u>Title</u>	<u>Page</u>
1	Schematic of Charged Colloid Generating System	4
2	Rayleigh Maximum Specific Charge as a Function of Drop Sizes	7
3	Specific Impulse as a Function of Charge-to-Mass Ratio for Various Accelerating Voltages Assuming Beam Uniformity	8
4	Dimensionless Source Field Vs. Dimensionless Current Density for Space Charge Flow Between Parallel Planes	12
5	Dimensionless Source Field and Current Density Vs. Space Charge Parameter, Ω , For Flow Between Parallel Planes	15
6	Charged Colloid Generating System Test Stand	22
7	Nozzle With a Small Flare	23
8	Nozzle With a Large Flare	24
9	Four Different Nozzles	25
10	High Speed Rotary Feedthrough	27
11	Nozzle Sprindle	28
12	Nozzle Spindle Showing Standoff Insulators and Insulated Coupling	29
13	Propellant Metering and Feed System	30
14	Rubber Analog of Nozzle and Accelerating Electrodes Showing Droplet Trajectory	32
15	Test Stand with Vacuum Chamber Bell Jar Removed	33

<u>Figure Number</u>	<u>Title</u>	<u>Page</u>
16	Extractor, Collector, and Target	34
17	View of Collector Window Showing Target, Target Grid and Target Shield	35
18	General Schematic of the Measurements	37
19	Test Stand with Instrumentation and Auxiliary Equipment	38
20	Volume Resistivity of Octoil with Tetra N Butyl Ammonium Picrate	41
21	Volume Resistivity of Glycerol with Sulfuric Acid	42
22	Volume Resistivity of Glycerol with Antimony Trichloride	43
23	Beam Current as a Function of Accelerating Voltage (Low Voltage Range) Insulating Cup	46
24	Beam Current as a Function of Accelerating Voltage (High Voltage Range) Insulating Cup	47
25	Beam Current as a Function of Accelerating Voltage with Liquid Metal	49
26	Extractor and Collector with Trace of Liquid Metal Beam	50
27	Target Mass Flow, Thrust and Current	51
28	Target Mass Flow, Thrust and Current as a Function of Accelerating Voltage	52
29	Target Mass Flow, Thrust and Current as a Function of Accelerating Voltage	53
30	Charge-to-Mass Ratio and Efficiency as a Function of Accelerating Voltage for Various Target Mass Flow Rates	54
31	Collector Current, I_c , Vs. Total Mass Flow, m_t , for Three Constant Voltages	56
32	Target Thrust, F_t , Vs. Target Mass Flow, m_t , for Three Constant Voltages	57

TABLE OF SYMBOLS

A	emission area
B	dimensionless parameter
C	dimensionless parameter
D	dimensionless parameter
E	electric field
E_o	electric field at edge of nozzle
F	thrust
F_t	thrust on target
I	current
I_c	collector current
I_{sp}	specific impulse
J	current density
L	nozzle-extractor distance
P	power
P_i	power of ideal engine
Q	electric charge
R	resistance
S	space-charge parameter
V	voltage
a	radius of droplet
d	distance
e_o	normalized electric field
h	film thickness
j	normalized current density
l	length
m	mass of droplet
m_t	target mass flow
m_T	total mass flow
\dot{m}	mass flow
q	charge of a droplet
r	radius of nozzle
t	time
v	exhaust velocity of propellant
α	angle of nozzle flare with axis
γ	surface tension
ϵ	capacitivity
η	efficiency
ν	kinematic viscosity
ρ	resistivity
ρ_m	mass density
σ	charge density
ω	angular velocity
Ω	space charge parameter

1. INTRODUCTION

In electrostatic thrusters, electrically charged particles of propellant are accelerated by a constant voltage. The propellant may consist of atomic or molecular ions or of matter in a colloidal state. Ion thrusters under development differ by the method used to generate the ions: in the contact ionization engine, a metal is ionized as it emerges from a porous material; in the electron bombardment engine, electrons partially contained by a magnetic field serve to ionize a metal vapor. Similarly, charged colloids are obtained by induction charging and by bombardment of a condensed vapor.

In the evaluation of an electrostatic thruster vis à vis a space mission, two parameters are particularly useful: the specific impulse and the efficiency. The specific impulse, I_{sp} , is defined by

$$I_{sp} = \frac{F}{\dot{m}g}$$

where F is the thrust, \dot{m} the propellant mass flow, and g , the acceleration of earth's gravity. The efficiency η , is the equivalent to the ratio of the power of an ideal engine with the same thrust and mass flow to the power of the actual engine.

From data analyzed recently (Reference 1), it appears that ion thrusters are efficient only at very high specific impulses, e.g., greater than 8,000 seconds. The electron bombardment thruster has an efficiency of only 60% for $I_{sp} = 4,000$ seconds. The contact ionization thrusters do not exceed 50% efficiency for I_{sp} lower than 6,000 seconds. This is not encouraging since for the first missions contemplated with electrostatic thrusters, the I_{sp} range of 1,700 to 4,000 seconds is the most desirable. Colloid thrusters, on the contrary, show promise of high efficiencies in this range.

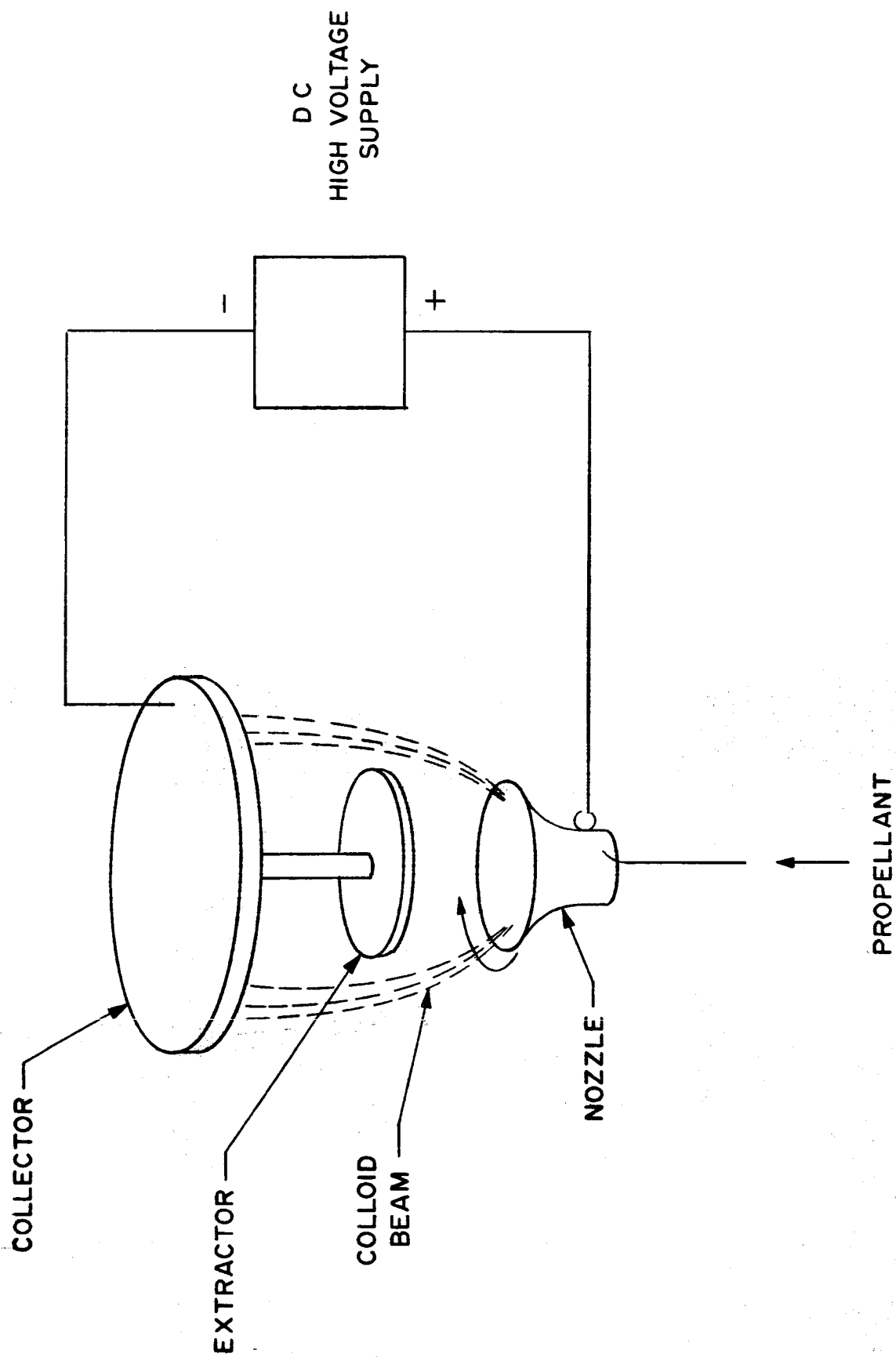
An examination of the induction charging method for colloids was undertaken and an analytical investigation accomplished by Cosmic, Inc. for the National Aeronautics and Space Administration (Reference 2). Charged colloids had been obtained by several previous investigators using liquids extracted from hollow needles by an electric field (induction charging). A summary of data obtained with this method of charging is shown on Table 1. In some cases, the beam obtained has one of the required characteristics inasmuch as measurements of the charge-to-mass ratio, q/m , of some droplets indicated the possibility of obtaining the required specific impulse with a still moderate accelerating voltage (10^5 volt.). However, the beam currents and mass flows obtained with

EXPERIMENTER	V (KV)	I (μa)	Q / m (COUL./sq)(kg/SEC)	m	NEEDLE DIA. (IN.)	DROPLET DIA. (μ)	PROPELLANT		ρ (g/cm)	MEASUREMENT METHOD (Q/M)
							BASE	ADDITIVE		
Space Technology Laboratories (References 3, 4, 5)	10		470		.005		Glycerol	7% SbCl ₃		Faraday Probe
	10		200		.005		Glycerol	3.5% SnCl ₄		Faraday Probe
	13		4.5			0.5	Octoil		$> 10^7$	
	6		12-80		.005-7		Woods Metal		5×10^{-5}	
		1-2	80		.005-.01	.05	Woods Metal		5×10^{-5}	Faraday Probe
Aerojet General Corp. (C. K. Hinrichs) (Reference 6)	6.8	1-2	60		.005-.01	.057	Liquid Metal			Faraday Probe
	6.0	1-2	12		.005-.01	0.15	Liquid Metal			Faraday Probe
	6.0	1-2	80		.005-.01		Liquid Metal			Faraday Probe
	10	1.0	180		.010		Glycerol	4% SbCl ₃		Massenfilter
	8.2	1.0	470		.010		Glycerol	7% SbCl ₃		Massenfilter
Aerojet General Corp. (C. K. Hinrichs) (Reference 6)	35		3-9				Octoil	4% TBAP	10^6	1/M
			0.2				Octoil S	1% TBAP	10^8	Faraday Probe
			1-4				Octoil	1% TBAP	10^7	Faraday Probe
	15		25				Octoil	4% TBAP	10^6	Faraday Probe
	25		.9-9				Octoil	4% TBAP	10^6	Faraday Probe
University of Illinois (C. D. Hendricks) (Reference 7)			8.8	1×10^{-5}	Wedge		Octoil	4% Picric Acid	10^7	Faraday Probe
	12		.06				Octoil			
	>12		1				Octoil			
	4		8				Glycerol			
Thiokol Chemical Corp. (D. M. Jamba) (Reference 8)			1-3		* Extraction from metal substrate	10-20	Aluminum			Time of Flight
	28.5		300			.003	Aluminum		3×10^{-6}	Instrument
	28.5		220,000			.002	Lead		10^{-5}	"
	20		465,000			.002	Lead		10^{-5}	"
			2,000				Copper		2×10^{-6}	"
Air Force (Hunter-Windman)	20		500				Glycerol	SO ₄ H ₂		Massenfilter
							Butyl- phthalate			Massenfilter
University of Illinois			10^5							

TABLE 1. SUMMARY OF RESULTS OF INDUCTION CHARGING OF COLLOIDS FROM NEEDLES. *

needles are extremely small. In order to obtain enough thrust for an actual space mission, an array of 10,000 to 100,000 needles would be required. Furthermore, as laboratory devices, needles are useful but the reliability of the data obtained is limited. More precisely, the data is limited to exploration of the beam by probes or massenfilters. Overall quantities such as beam current, mass flow, and thrust are difficult or impossible to measure. In brief, even as a tool to analyze the droplet formation, the needles are not very suitable because of their very low output. It was concluded that better results might be obtained by creating the droplets on an edge rather than at a point and for this purpose, a spinning nozzle was utilized. A schematic view of the system is shown in Figure 1. A liquid propellant is fed inside a spinning nozzle and spread on the inner surface of the nozzle by centrifugal force. In the absence of an electric field, the liquid is atomized in small droplets (size 1 to 100 microns) in front of a plane perpendicular to the nozzle axis. A system of two electrodes is placed in front of the nozzle so as to create an intense electric field on the edge. Under the action of the field, electric charges are attracted to the surface of the liquid thereby causing the droplets to be charged as they are leaving the edge. In this arrangement, it is possible to change the geometry in order to obtain different beam configurations. It is also possible to vary independently the nozzle rotating speed, the voltage, and the propellant mass flow. Overall characteristics of the beam (current, mass flow on collector, etc.) may be monitored continuously during test; there is no beam interception by the extracting electrode.

A one year analytical and experimental program was conducted at Cosmic, Inc., and a rotating nozzle has been operated successfully. The results of this program are related in this report. The following sections will be devoted first to an analytical investigation, then to a description of the system and its instrumentation, to a presentation and a discussion of the experimental data, and finally, conclusions will be drawn.



SCHEMATIC OF CHARGED COLLOID GENERATING SYSTEM

FIGURE 1

2. ANALYTICAL INVESTIGATION OF THE CHARGED COLLOID SYSTEM

The mechanism whereby a liquid propellant is made to coat the inside of a spinning nozzle, is spun off the edge of the nozzle by the combined action of the centrifugal and electrostatic forces and finally accelerated as a charged beam is not completely amenable to calculations. In this section, detailed analysis, supplemented, as necessary, by qualitative and semi-quantitative arguments, is employed to explain and predict system performance.

2.1 Film Flow Inside the Nozzle

The spinning nozzle should provide a flow of liquid to form a ring as thin as possible at the edge of the nozzle. Under the assumption that the liquid is being spread inside the cup uniformly around the circumference, the flow of the liquid toward the edge of the nozzle is then governed by the Navier-Stokes laminar viscous flow equations (Reference 2). Under the further assumption that the propellant wets the nozzle, it is possible to derive an expression relating the mass flow, \dot{m} , to the film thickness, h . For an ideal nozzle which would consist of a cone of half angle, α , the relation is as follows:

$$\dot{m} = (2\pi/3) (\sin \alpha) \rho_m^2 r^2 \omega^2 h^3 / \nu$$

where r and ω are the radius and angular velocity, respectively, of the nozzle, and ρ_m and ν are the density and viscosity respectively of the propellant.

Thus it is seen that the film thickness varies as the $1/3$ power of the mass flow, but as the $2/3$ power of the radius and angular velocity.

2.2 Qualitative Explanations of Droplet Formation

Analytical investigation of the action of an electric field on an interface between a liquid and a vacuum (Reference 2) can only be fragmentary. We shall, therefore, limit ourselves here to a qualitative interpretation. Assuming that regularly spaced protuberances of the liquid occur around the edge of the nozzle, as they extend outwards, the lines of force of the electric field tend to concentrate on them so that cusps are formed which in turn tend to be unstable and separate into droplets. This mechanism of droplet formation has never been observed at the edge of the nozzle, but has been observed visually at Cosmic, Inc. in the case of a layer of liquid which is deposited on a flat electrode and is pulled off by an electric field.

2.3 Limit on Droplet Size and Charge-to-Mass Ratio

Charging of the liquid propellant is accomplished by conduction. (It should be noted that the term "electrophoresis" sometimes used in describing droplet charging is simply a synonym for ionic conduction). According to the mechanism explained in the previous section, the cusps form one electrode of the system and the charges are attracted to the tips of the cusps as they constitute the part of the electrode where the field is the most intense. The actual charge on the tip of the cusp is determined by hydrodynamic phenomena, which cannot be conveniently analyzed. It is possible, however, to calculate an upper limit on the droplet charge. For a liquid of surface tension γ , the electrostatic forces tend to increase the size of the droplet whereas the surface tension forces tend to shrink it. Rayleigh (Reference 11) has shown that stable equilibrium corresponds to equal electrostatic and surface tension forces. This yields for the charge-to-mass ratio of a spherical drop of radius a ,

$$q/m = 6 \left(\epsilon_o \gamma \right)^{1/2} / \rho_m a^{3/2}$$

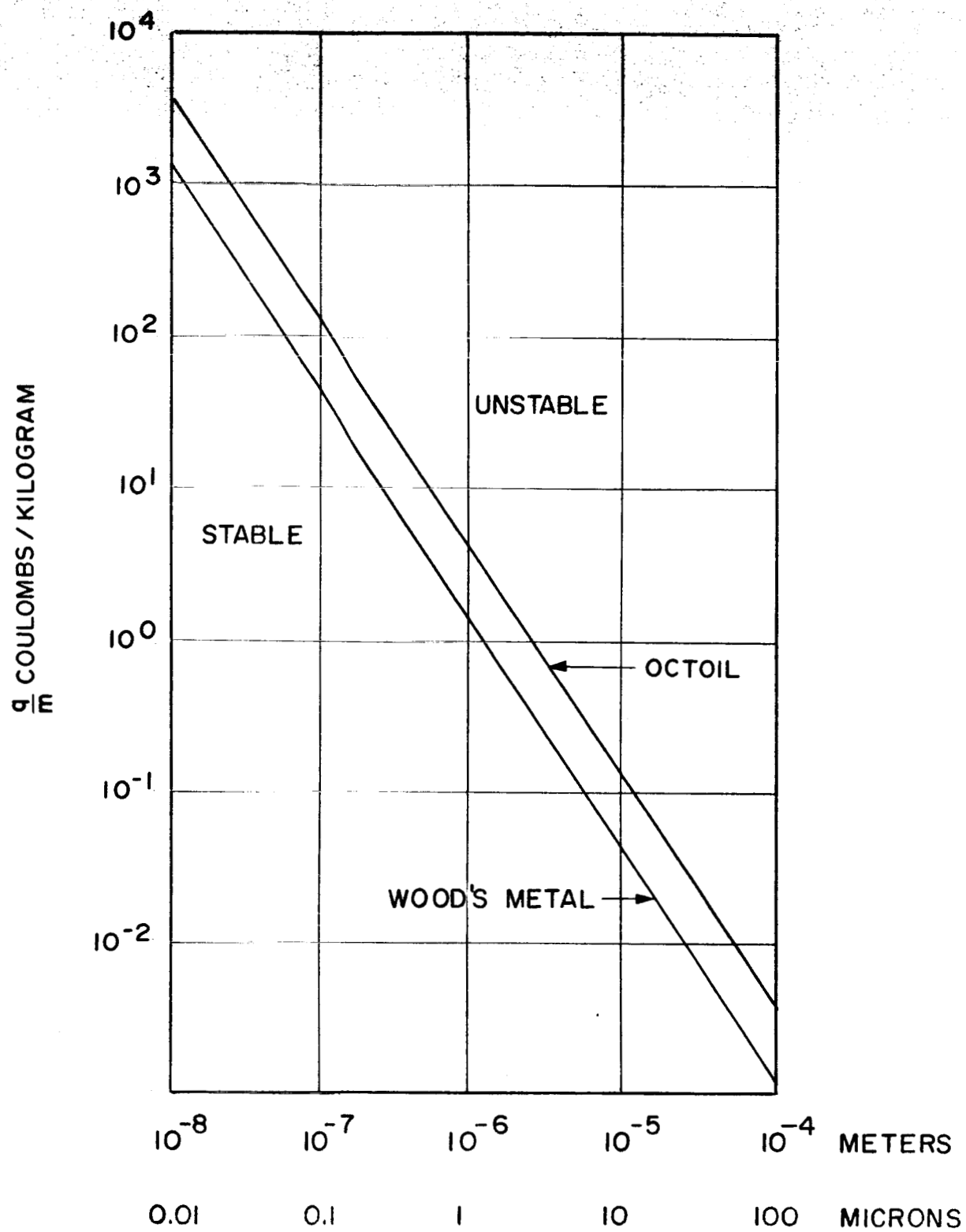
This relation is plotted in Figure 2 for Wood's metal, and for octoil. It appears that in order to obtain charge-to-mass ratios in the desired range of 100 to 1,000 coulombs per kilogram, it is necessary for the particles to be smaller than one-tenth of a micron in radius. The range of charge-to-mass ratio corresponding to a range of specific impulse is defined in Figure 3. It should be noted that while the problem of corona at the edge of the nozzle might occur in test in air or in a poor vacuum, this problem does not occur in a good vacuum and consequently shall not be considered here.

2.4 Effect of Propellant Conductivity

The analysis accomplished above suggests that the ideal propellant would be one having an infinite conductivity so that regardless of the speed at which the cusps are being formed and at which they move outward, the charge density on the surface of the cusp is proportional to the electric field. Let's analyze the case of a liquid with a finite conductivity. For this purpose, we shall define as Q_∞ , the charge which would exist in a given volume of the cusp if the cusp were to keep the same shape indefinitely and, Q_t , the charge at time, t . In this case, we have

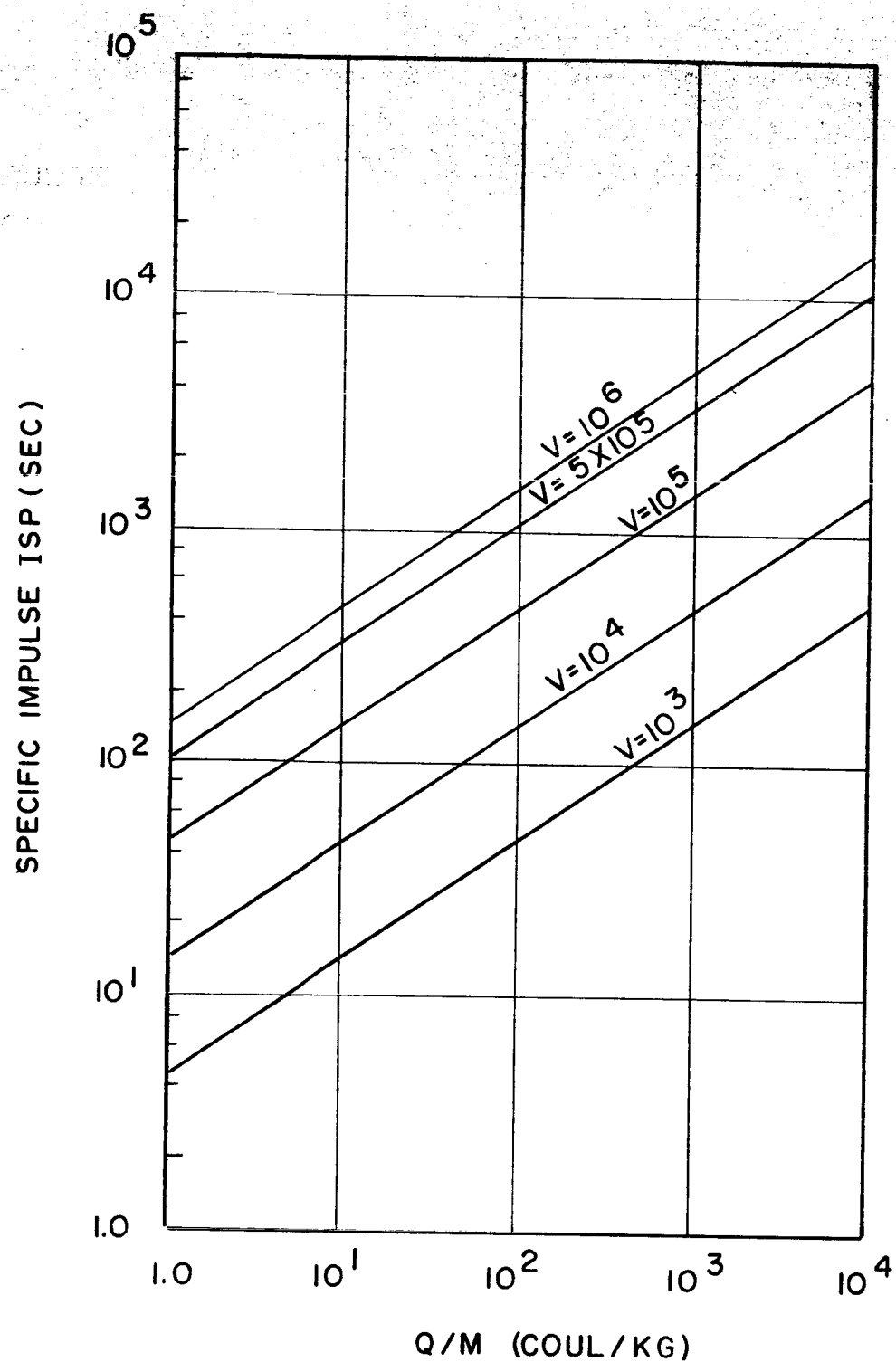
$$Q_t = Q_\infty \left(1 - e^{-\frac{t}{\epsilon \rho}} \right)$$

in which ϵ and ρ are the capacitivity and resistivity of the propellant.



RAYLEIGH MAXIMUM SPECIFIC CHARGE AS A FUNCTION OF DROP SIZES

FIGURE 2



SPECIFIC IMPULSE AS A FUNCTION OF CHARGE-TO-MASS RATIO FOR VARIOUS ACCELERATING VOLTAGES ASSUMING BEAM UNIFORMITY

FIGURE 3

The product, $\epsilon \rho$, which is called the dielectric relaxation time of the liquid, is therefore a measure of the time it takes for the charges to move to the tip of the cusp. It is much more difficult to find a suitable estimate of the time during which the droplet is being charged, i.e., the time during which the droplet is still a part of the cusp and is submitted to the field. An order of magnitude estimate of such a time may be made by calculating the time which it takes a hypothetical particle of charge-to-mass ratio $\frac{q}{m}$ to travel a distance $d = 1$ drop diameter when leaving the nozzle with no initial velocity. This time is given as a function of the field E by:

$$d = 1/2 \frac{q}{m} E t^2 \quad \text{or}$$

$$t = \left(\frac{2d}{\frac{q}{m} E} \right)^{1/2}$$

It is important to realize that such a time may only be used for an "order of magnitude" estimate since it does not take into account:

- the viscosity of the liquid,
- the fact that the field is a function of the droplet shape, or
- the fact that there is an initial velocity with both axial and tangential components.

The effect of these "unaccounted for" factors would be to both increase and decrease the estimate of the time t .

For the plausible numerical values

$$\epsilon = 10^{-11} \text{ farad/m} \quad \rho = 1.5 \times 10^6 \text{ ohm-cm} = 1.5 \times 10^4 \text{ ohm-m}$$

$$d = 10^{-7} \text{ m} \quad E = 10^7 \text{ volt/m}$$

$$q/m = 10^2 \text{ coul/kg}$$

We obtain

$$t = 1.4 \times 10^{-8} \text{ sec}$$

$$\epsilon \rho = 1.5 \times 10^{-7} \text{ sec}$$

It appears therefore that for these plausible numerical values, the actual charge would be considerably smaller than that which an infinitely conducting liquid droplet would have. The importance of the liquid conductivity will be further clarified later on in this report in the analysis of the test data.

2.5 Parametric Study of System Operation, Including Space-Charge Effects

It has long been recognized that space-charge phenomena not only limit the maximum thrust attainable with an electrostatic propulsion system but also prohibit any sustained thrust whatsoever, unless the charged particle stream is adequately neutralized. Although the influence of these two fundamental constraints upon the performance of ion engines has been studied extensively and is reasonably well understood, the role of space-charge in colloidal engines is more obscure. For example, in the type of charged colloid generating system being studied here, the electric field established between the nozzle and the electrodes serves both to induce a charge on the droplets and to accelerate them. Consequently, a conventional Child-Langmuir type space-charge limit is inapplicable here, because in such a limit, the electric field at the nozzle vanishes and thus creates no charged droplets. During this program, this problem has been analyzed and the results are summarized below.

The influence of space-charge can be interpreted operationally in the following fashion. In the system considered here, the experimentalist can select the nozzle and electrode geometries, the propellant, the nozzle angular velocity, ω , the accelerating voltage, V , and the mass flow rate, \dot{m} . Thus, for example, a series of experiments can be performed in which the mass flow rate alone is varied. For a sufficiently small flow rate, the electric field at the nozzle is essentially the vacuum field, droplets are created with a relatively high charge-to-mass ratio, q/m , and a relatively small current is set up. As the flow rate increases, the current increases and the attendant space-charge decreases the field at the nozzle and thereby decreases the charge-to-mass ratio of the individual droplets. It is clear that further increases in mass flow rate continually decrease the charge-to-mass ratio. The variation of the current density, J , current, I , and thrust, F , with flow rate is, however, not obvious but can and will be predicted below. Although the space-charge influence upon system performance can be demonstrated most easily, perhaps, by varying the mass flow rate, this influence must also be demonstrable by varying the voltage or, indeed, any of the controllable experimental elements. The variation of system performance with variations in these controllable elements can be predicted as follows.

It is clear that for any space-charge flow, the electric field, E_0 , at the source of charged particles decreases from the vacuum field, E_0^* , to zero as the current density, J , between the source and the accelerating electrode increases from zero to the space-charge-limited current density, J^* . Moreover, this variation can conveniently be described in terms of

the normalized field, e_o , and the normalized current density, j , where

$$e_o \equiv E_o / E_o^*$$

$$j \equiv J / J^*$$

Thus, for example, for a space-charge flow of particles with charge-to-mass ratio, q/m , passing between parallel plane electrodes separated by a distance, L , and a potential difference, V ,

$$E_o^* = V/L$$

$$J^* = \frac{4}{9} \frac{\epsilon_o (2 q/m)^{1/2} V^{3/2}}{L^2}$$

where ϵ_o = capacitivity of free space. Moreover, it is readily shown that for this space-charge flow, e_o and j are related by

$$j = 1/2 \left[1 \pm \left\{ 1 - \frac{27}{4} e_o^2 (1 - e_o) \right\}^{1/2} \right] \quad \begin{matrix} 0 \leq e_o \leq 2/3 \\ 2/3 \leq e_o \leq 1 \end{matrix}$$

This relationship is derived in the Appendix and depicted in Figure 4. The significant points here are that, for any space-charge flow, i) the normalizing field, E_o^* , and current density, J^* , must, by dimensional analysis, have the form

$$E_o^* = V/L$$

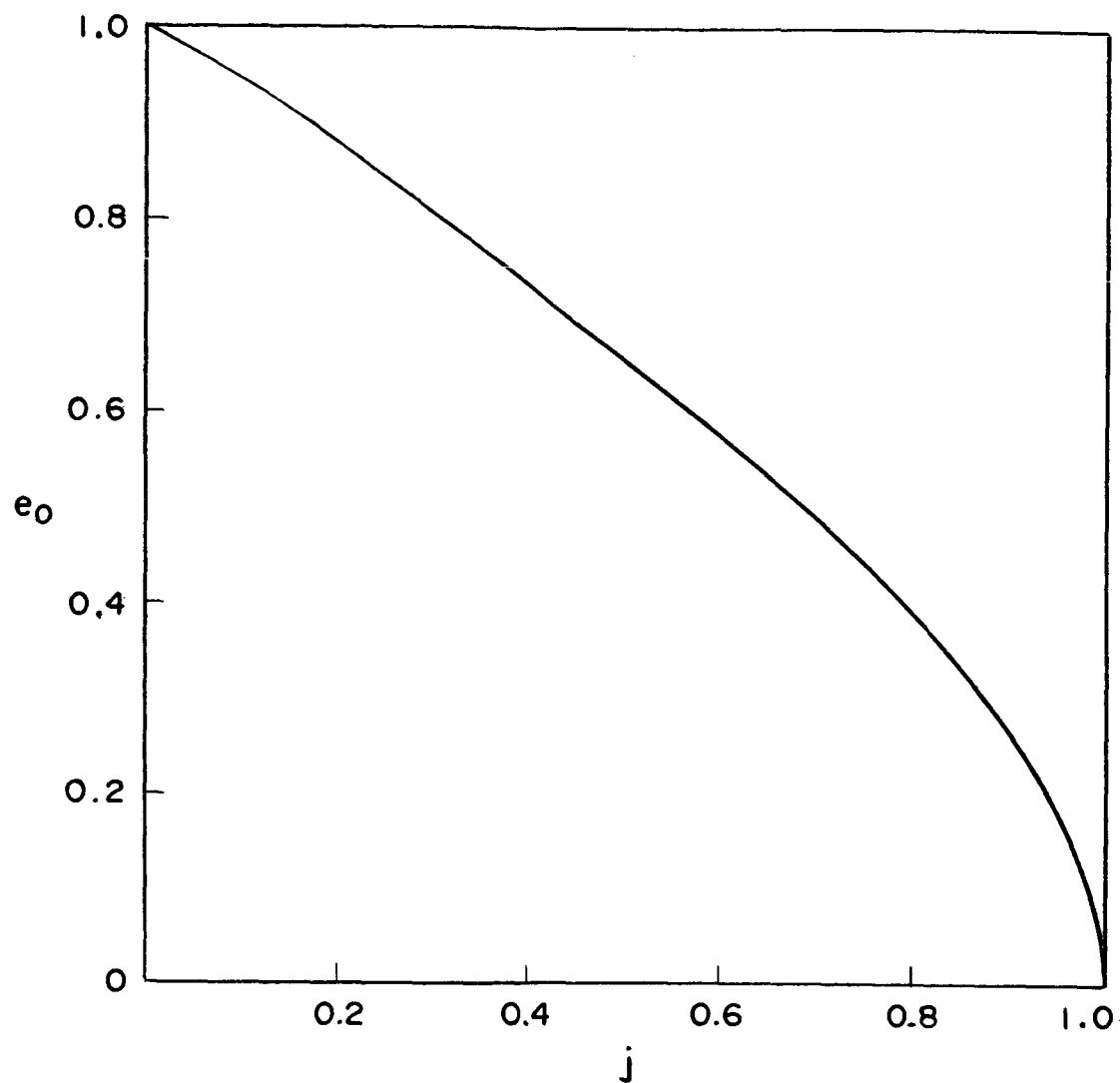
$$J^* = B \epsilon_o (q/m)^{1/2} V^{3/2} / L^2$$

where L is a characteristic length of the electrode system (e.g., the electrode separation, for the parallel-plane geometry) and B is a dimensionless parameter dependent upon electrode geometry (e.g., $B = 4/2/9$ for the parallel-plane geometry), ii) it is possible to establish a relation between e_o and j and, iii) this relation satisfies

$$e_o (j = 0) = 1$$

$$e_o (j = 1) = 0$$

In particular, for the colloidal generating system considered here, such a relation exists and weak space-charge effects correspond to small currents, i.e., $j \ll 1$, and large space-charge effects correspond to large currents, i.e., $e_o \ll 1$.



DIMENSIONLESS SOURCE FIELD, e_0 , VS
DIMENSIONLESS CURRENT DENSITY, j ,
FOR SPACE CHARGE FLOW BETWEEN
PARALLEL PLANES.

FIGURE 4

We recall that, for any electrostatic thruster,

$$J = (\dot{m}/A) (q/m)$$

$$I = \dot{m} (q/m)$$

$$F = \dot{m} (2V)^{1/2} (q/m)^{1/2}$$

where A is the emissive area, and the charge-to-mass ratio is assumed to be homogeneous. For convenience, we retain that assumption in this discussion, since the modifications required to incorporate inhomogeneities are perfectly straightforward. Since the droplets are charged by induction, their charge-to-mass ratio is proportional to the electric field at the edge of the nozzle, and, therefore,

$$q/m = (\hat{q}/m) e_o$$

where (\hat{q}/m) depends solely on controllable experimental elements, i.e., geometry, propellant, ω , V , \dot{m} . Consequently,

$$J = (\dot{m}/A) (\hat{q}/m) e_o \equiv \hat{J} e_o$$

$$I = \dot{m} (\hat{q}/m) e_o \equiv \hat{I} e_o$$

$$F = \dot{m} (2V)^{1/2} (\hat{q}/m)^{1/2} e_o^{1/2} \equiv \hat{F} e_o^{1/2}$$

where the normalizing terms, \hat{J} , \hat{I} , \hat{F} likewise depend solely on controllable elements. To emphasize the generality of this approach, the formal expressions for these normalizing terms are retained, with explicit representations of them being derived later.

We are now in a position to calculate space-charge effects, since the preceding equations imply

$$\begin{aligned} j &\equiv \frac{I}{J^*} = \frac{(\dot{m}/A) (q/m)}{B \epsilon_o (q/m)^{1/2} V^{3/2}/L^2} \\ &= (q/m)^{1/2} \frac{(\dot{m}/A) L^2}{B \epsilon_o V^{3/2}} \\ &= e_o^{1/2} \frac{(\hat{q}/m)^{1/2} (\dot{m}/A) L^2}{B \epsilon_o V^{3/2}} \end{aligned}$$

Thus, we derive the equivalent results

$$\Omega = e_o^{-1} j^2 \quad e_o = j^2 \Omega^{-1} \quad j = e_o^{1/2} \Omega^{1/2}$$

where

$$\Omega \equiv (\hat{q}/m) \frac{(\dot{m}/A)^2 L^4}{B^2 \epsilon_o^2 V^3}$$

and Ω depends solely on controllable elements. It follows that weak space-charge effects (i.e., $e_o \approx 1$, $j \ll 1$) correspond to

$$\Omega = e_o^{-1} j^2 \approx j^2 \ll 1$$

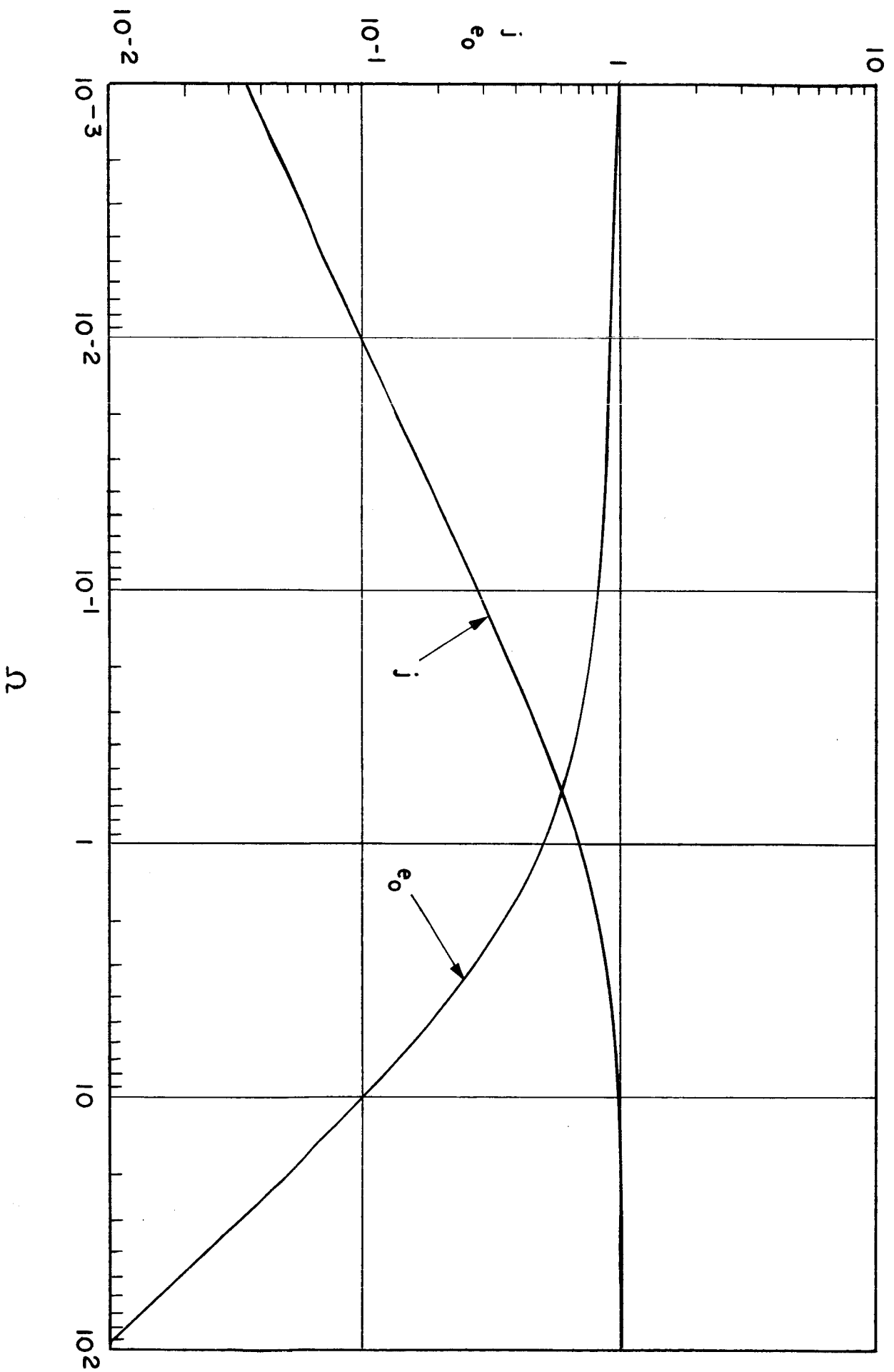
whereas strong space charge effects (i.e., $e_o \ll 1$, $j \approx 1$) correspond to

$$\Omega = e_o^{-1} j^2 \approx e_o^{-1} \gg 1$$

Thus, the influence of space-charge upon system performance is dictated solely by the value of the dimensionless parameter Ω , which, in turn, is determined completely by the experimenter's choice of geometry, propellant, \dot{m} , ω , V . For small Ω (i.e., $\Omega \ll 1$), space-charge effects are weak; with increasing Ω , they are enhanced until, for $\Omega \gg 1$, they become dominant. Figure 5 shows the variation of the dimensionless source field, e_o , and current density, j , with the parameter Ω , for the parallel-plane geometry. Since e_o and j are monotonically interrelated, the trend shown in Figure 5 is applicable to all space-charge flows; moreover, the asymptotic behavior for large and small Ω is completely general.

In order to clarify the general results derived above, we shall now specialize them by making further assumptions. In particular, we assume that the film thickness, h , at the edge of the nozzle may be taken as a characteristic droplet size, so that

$$\begin{aligned} (\hat{q}/m) &= \frac{(\text{surface charge density})}{(\text{mass density})} \frac{(\text{droplet surface area})}{(\text{droplet volume})} \\ &= \frac{C \epsilon_o V}{\rho_m h L} \end{aligned}$$



DIMENSIONLESS SOURCE FIELD, e_0 , AND CURRENT DENSITY, j , VS SPACE CHARGE PARAMETER, Ω , FOR FLOW BETWEEN PARALLEL PLANES.

FIGURE 5

where ρ_m is the mass density of the propellant, and C is a dimensionless parameter which depends upon geometry and which is large compared to 1 because of the nozzle's sharp edge and the resulting enhancement of the electric field. We further assume that the film thickness is given (cf. Reference 2) by

$$h = \left(\frac{\nu \dot{m}}{D \rho_m r^2 \omega^2} \right)^{1/3}$$

where

ν = kinematic viscosity of the propellant

r = radius of the nozzle at its edge

D = dimensionless parameter which depends upon nozzle geometry and is typically of order 1.

Since the emissive area is

$$A = 2 \pi r h$$

these assumptions permit us to conclude that

$$(\hat{q}/m) = D^{1/3} \frac{C \epsilon_0 V}{L} \left(\frac{r^2 \omega^2}{\rho_m^2 \nu \dot{m}} \right)^{1/3}$$

$$\hat{J} = D^{2/3} \frac{C \epsilon_0 V}{L} \left(\frac{r \omega^4 \dot{m}}{\rho_m \nu^2} \right)^{1/3}$$

$$\hat{I} = D^{1/3} \frac{C \epsilon_0 V}{L} \left(\frac{r^2 \omega^2 \dot{m}^2}{\rho_m^2 \nu} \right)^{1/3}$$

$$\hat{F} = D^{1/6} \left(\frac{2 C \epsilon_0}{L} \right)^{1/2} V \left(\frac{r^2 \omega^2 \dot{m}^5}{\rho_m^2 \nu} \right)^{1/6}$$

and that the space-charge parameter Ω has the form

$$\Omega = \frac{C D}{(2 \pi B)^2} \left(\frac{\dot{m} \omega^2 L^3}{\epsilon_o V \nu} \right)$$

It should be noted that the normalizing (i.e., "hatted") terms and the parameter Ω depend solely and explicitly upon controllable experimental elements.

It follows directly from the results derived above that for $\Omega \ll 1$, space-charge effects are weak and (q/m) , J , I , and F behave like their "hatted" counterparts. Conversely for $\Omega \gg 1$, space-charge effects are strong, $e_o \approx \Omega^{-1}$, and

$$(q/m) = (\hat{q}/m) \Omega^{-1} = D^{-2/3} (2 \pi B)^2 \frac{\epsilon_o^2 V^3}{L^4} \left(\frac{r \nu}{\rho_m \omega^2 \dot{m}^2} \right)^{2/3}$$

$$J = \hat{J} \Omega^{-1} = D^{-1/3} (2 \pi B)^2 \frac{\epsilon_o^2 V^3}{L^4} \left(\frac{r \nu}{\rho_m \omega^2 \dot{m}^2} \right)^{1/3}$$

$$I = \hat{I} \Omega^{-1} = D^{-2/3} (2 \pi B)^2 \frac{\epsilon_o^2 V^3}{L^4} \left(\frac{r^2 \nu^2}{\rho_m \omega^4 \dot{m}} \right)^{1/3}$$

$$F = \hat{F} \Omega^{-1/2} = D^{-1/3} 8^{1/2} \pi B \frac{\epsilon_o V^2}{L^2} \left(\frac{r \nu \dot{m}}{\rho_m \omega^2} \right)^{1/3}$$

For the operationally interesting situation wherein the geometry and propellant are not changed but the angular velocity, mass flow, and voltage are varied, we have the following conclusions. For $\Omega \ll 1$, space charge effects are weak and

$$q/m \sim \omega^{+2/3} \dot{m}^{-1/3} V$$

$$J \sim \omega^{+4/3} \dot{m}^{+1/3} V$$

$$I \sim \omega^{+2/3} \dot{m}^{+2/3} V$$

$$F \sim \omega^{+1/3} \dot{m}^{+5/6} V$$

Conversely, for $\Omega \gg 1$, space-charge effects are strong and

$$\begin{aligned} q/m &\sim \omega^{-4/3} \dot{m}^{-4/3} V^3 \\ J &\sim \omega^{-2/3} \dot{m}^{-2/3} V^3 \\ I &\sim \omega^{-4/3} \dot{m}^{-1/3} V^3 \\ F &\sim \omega^{-2/3} \dot{m}^{+1/3} V^2 \end{aligned}$$

Thus, at sufficiently low voltages, system outputs rise rather steeply (like V^2 or V^3) with increasing voltage; as voltage increases, the outputs tend to rise less steeply until ultimately they vary linearly with V . For sufficiently small angular velocities, all outputs increase with increasing angular velocity; conversely, for sufficiently large angular velocities, the outputs decrease with increasing ω . Thus, for each output, there is an optimal angular velocity which maximizes that output. The variation of system outputs with mass flow is somewhat more complicated. The charge-to-mass ratio steadily decreases with increasing mass flow, and at a steeper rate for larger \dot{m} . The current and current density initially increase and then ultimately decrease with increasing mass flow. The thrust increases steadily with increasing mass flow, but at a slower rate for larger \dot{m} . It should be noted that all of these predicted trends are, of course, verifiable experimentally.

Comparison of experimental data with the theoretical predictions derived above is facilitated by deleting the dimensionless parameters B , C , D which cannot be determined accurately. Thus, instead of employing the actual space-charge parameter Ω , which contains B , C , and D , we would use the measurable parameter S , defined by

$$S \equiv \frac{\dot{m} \omega^2 L^3}{\epsilon_0 V^2 v}$$

Similarly, new normalizing terms (\hat{q}/\hat{m}) , \hat{J} , \hat{I} , and \hat{F} are defined by deleting B , C , D wherever they appear in (q/m) , J , I , F above. In this way, it becomes possible to plot I/\hat{I} and F/\hat{F} vs. S , and to determine whether the anticipated shape (though not, of course, the magnitude) of e_0 and $e_0^{1/2}$ vs. Ω is obtained.

In summary, then, a general method for estimating space-charge effects has been derived. In its most general form, this method is based solely upon the existence of the space-charge flow and upon the induction

mechanism of droplet charging. As an illustration of how the general theory can be applied, specific plausible assumptions regarding droplet charging were introduced and used to predict experimentally verifiable trends of system performance. It seems appropriate to compare these specific trends with the data, before introducing alternative or more refined assumptions within the framework of the general theory. This comparison will be made in Section 4.

2.6 Relation Between the Measured and Calculated Performance Characteristics

In this section we shall analyze the relationships that exist between the measured quantities and the calculated characteristics which are used to evaluate the system.

The quantities obtained from test data are:

Beam current	I
Beam mass flow	\dot{m}
Accelerating voltage	V
Thrust	F

The characteristic quantities which are of interest for the evaluation of the system are

Power	P
Efficiency	η
Charge-to-mass ratio	q/m
Specific impulse	I_{sp}

We shall examine each of these quantities separately:

Power: We shall neglect the power require to rotate the nozzle and the power loss of the propellant feed system. Under these conditions, the input power is given by

$$P = VI$$

Efficiency: Tests have shown that all the propellant supplied to the nozzle is charged and utilized, therefore, the utilization efficiency is virtually 100%. Hence, the efficiency η is equal to the electrical efficiency, i.e., the ratio of the power P_i of an ideal engine having the same thrust and mass flow to the actual power P . Thus

$$\eta = \frac{P_i}{P} = \frac{F^2 / 2 \dot{m}}{VI} = \frac{F^2}{2 VI \dot{m}}$$

Consequently, the efficiency can be readily determined from the four measured quantities, without any additional data, e.g., the actual distribution of q/m . This results in a great simplification as compared to the complex derivation otherwise required. (Reference 9). The expression for η stresses the need for accurate measurements: if the error on F , \dot{m} , I and V is 5%, the cumulated error on η is 25%.

Charge-to-Mass Ratio: The charge-to-mass ratio q/m is not, in general, homogeneous but may only be described by its distribution function. The Faraday probe and the massenfilter which analyze the beam may provide information about the actual distribution of charge-to-mass ratio. On the other hand, the measurements of F , I , V , \dot{m} yield moments of the distribution as follows:

If $f\left(\frac{q}{m}\right) d\left(\frac{q}{m}\right)$ is the beam current of the particles having a charge-to-mass ratio between (q/m) and $(q/m) + d(q/m)$ the mass flow and the thrust will be given by:

$$\begin{aligned} \dot{m} &= \int \left(\frac{q}{m}\right)^{-1} f\left(\frac{q}{m}\right) d\left(\frac{q}{m}\right) \quad \text{and} \\ F &= \left(2V\right)^{1/2} \int \left(\frac{q}{m}\right)^{-1/2} f\left(\frac{q}{m}\right) d\left(\frac{q}{m}\right) \end{aligned}$$

thus it is possible to know the average and the moments of order -1 and - 1/2 of the current distribution.

3. DESCRIPTION OF COLLOID GENERATING SYSTEM AND INSTRUMENTATION

3.1 Colloid Generating System

The primary consideration in the design of the system was flexibility. The system is so designed that changes in the accelerating voltage, mass flow, nozzle rotating speed and system geometry can easily be effected. The maximum period of operation varies from two minutes to fifty minutes depending upon the mass flow. With the exception of the propellant metering and feed system and the nozzle drive motor all the components are located inside the vacuum chamber, as shown in Figure 6. The various components of the system will be described below.

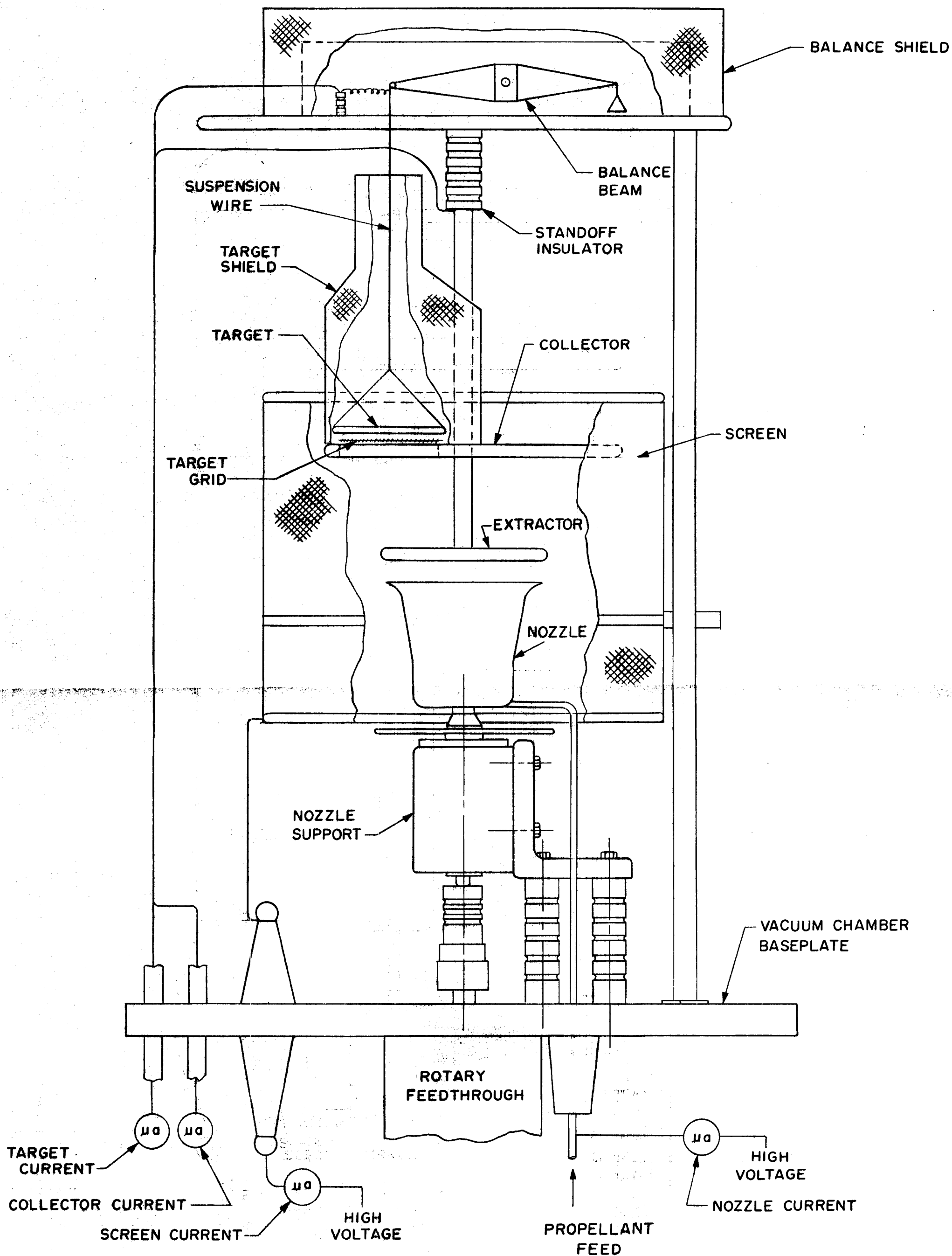
3.1.1 Nozzle

Two typical nozzles are shown in Figures 7 and 8. The delivery of the liquid propellant in the nozzle presented a problem. To achieve the desired flow characteristics, the cup was constructed with two sections, connected by a series of holes. The propellant is supplied in the rear section by a feed tube as shown in Figure 7. The centrifugal force causes the propellant to flow to the sides of this section of the nozzle and when sufficient liquid accumulates to exceed the level of the shoulder it flows through the holes into the forward section. The shoulder prevents the flow from being greater through certain holes than through the others due to the possibility that all the holes might not be exactly positioned with respect to the axis. The liquid flows evenly through the holes into the front section of the nozzle and then to the sides of this section. A short straight section allows the liquid emerging from the holes to unite and form a continuous film. This film flows toward the edge of the nozzle at an increasing rate of speed determined by the flare so that the film at the edge is thinner than at the base.

The choice of the nozzle material is governed primarily by the requirement that the liquid propellant wet the nozzle. The nozzle in Figure 7 was first made of solid aluminum and later plated with silver. The nozzles shown in Figure 8 were made of an insulating material, of aluminum later plated with silver and of brass. These and a nozzle with a small flare are shown in Figure 9.

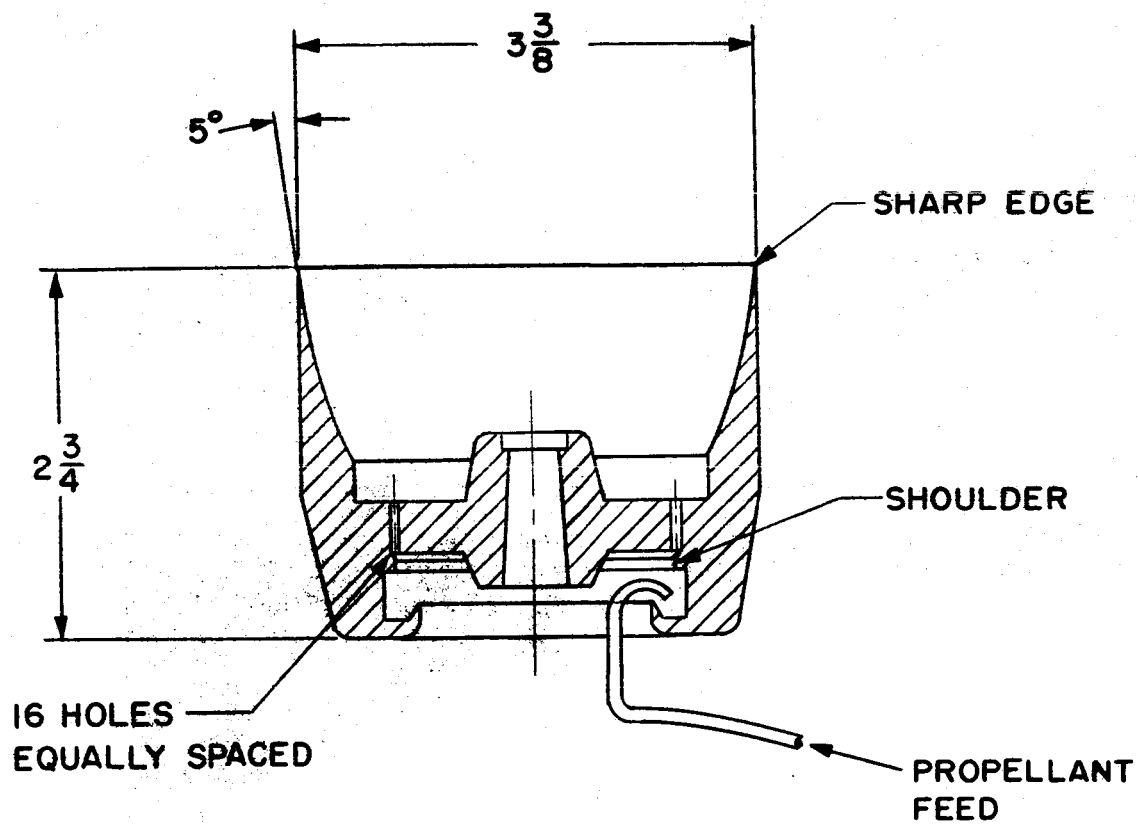
3.1.2 Nozzle Spindle and High Speed Feedthrough

It is not practical to utilize an electric motor inside the vacuum chamber. Since no rotary feedthrough was available

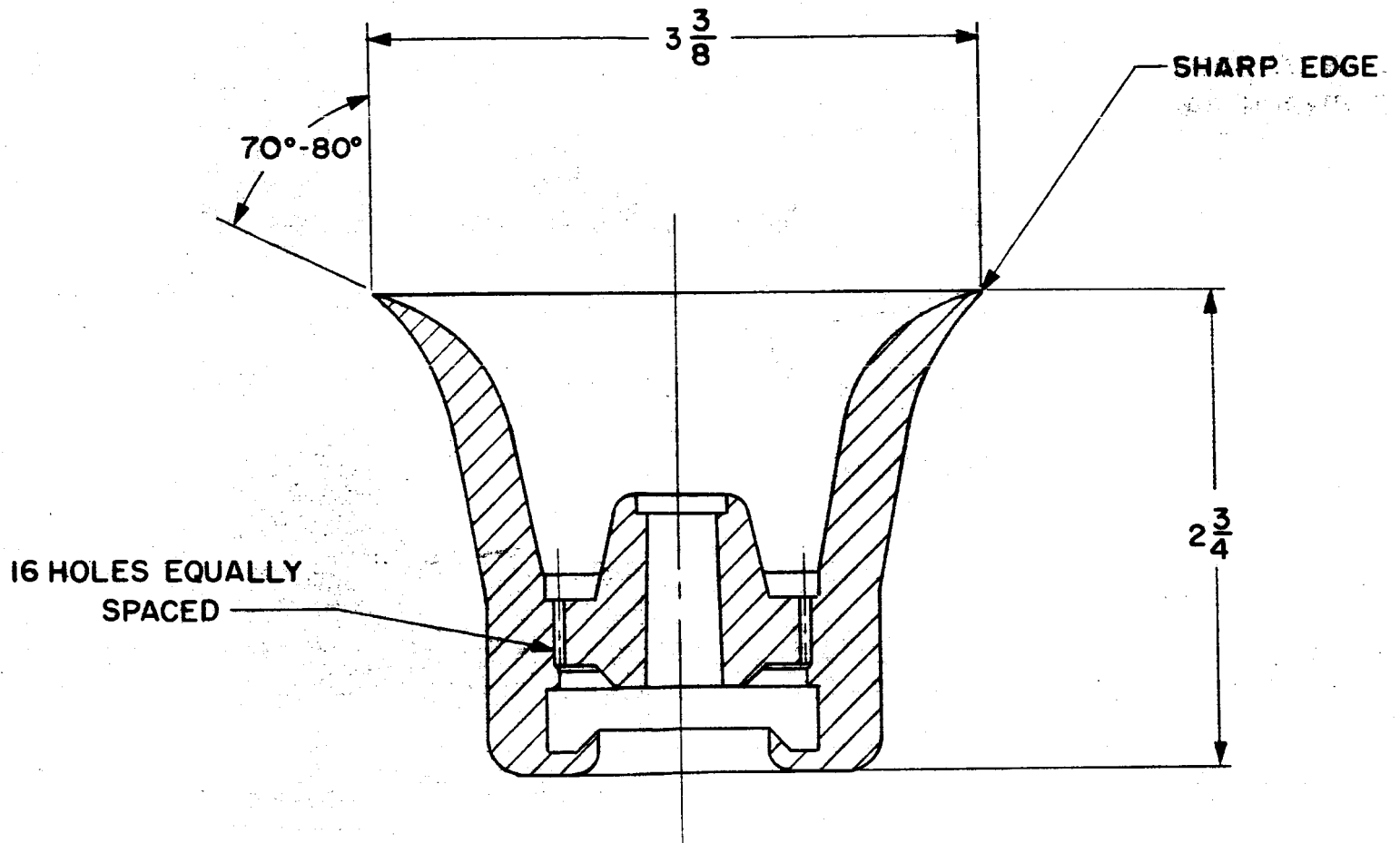


CHARGED COLLOID GENERATING SYSTEM TEST STAND

FIGURE 6



NOZZLE WITH A SMALL FLARE
FIGURE 7



NOZZLE WITH A LARGE FLARE

FIGURE 8



Aluminum,
Large Flare

Insulating,
Large Flare

Small Flare

Brass, Large Flare

Figure 9. Four Different Nozzles

which could operate at speeds higher than 600 rpm, one had to be developed in the course of this program. A disassembled view of this feedthrough system is shown in Figure 10. Shown from left to right is the electric motor, the housing, the rotating magnet, adapting flange, the cylinder which forms the barrier between the atmosphere and the vacuum, and finally, the rotor which operates in the vacuum. The whole assembly attaches to the vacuum chamber baseplate.

Since the nozzle must be operated at high voltage, it must be suitably insulated. In addition, since it will be operated at speeds up to 15,000 rpm, a rigid mounting is required. A special nozzle spindle was made which is shown in Figures 11 and 12. The bearings are preloaded with the top bearing securely clamped and the bottom bearing free to move with temperature changes in the system. Four standoff insulators and an insulated coupling between the rotary feedthrough and the spindle provide sufficient insulation for better than 60 kilovolts in vacuum.

The four bearings operating in vacuum (two in the feedthrough and two in the spindle) are precision bearings (ABEC 7 or better) lubricated by a suspension of molybdenum disulphide in octoil or silicon vacuum grease. The performance of the bearings was excellent. One bearing in the feedthrough had to be replaced and once the preload was adjusted no bearing replacement was required for the spindle.

The drive system enabled the nozzle to be rotated continuously up to 10,000 rpm and intermittently up to 18,000 rpm, the limit of the drive motor. Continuous operation at speeds in excess of 10,000 rpm would require the addition of a cooling system.

3.1.3 Propellant Metering and Feed System

The propellant metering and feed system is shown in Figure 13. The propellant to be used for a test is drawn from the reservoir, a 50 ml syringe, into the glass metering tube. A pinchcock is applied to the reservoir and the feed line to the nozzle is opened. A piston driven by a synchronous motor delivers the propellant at a constant flow rate. A series of synchronous motors with speeds of 6, 12, 30, 60, and 120 rpm permit operation of the system with a propellant having a density of $1,000 \text{ kg/m}^3$ at mass flow rates of 1.5×10^{-6} , 3.0×10^{-6} , 7.5×10^{-6} , 15×10^{-6} , $30 \times 10^{-6} \text{ kg/sec}$.

The metering and feed system must be able to be operated at high voltage. With the exception of the piston, screw and synchronous motor drive, all the components are made of insulating material and the system is mounted on an insulating board.

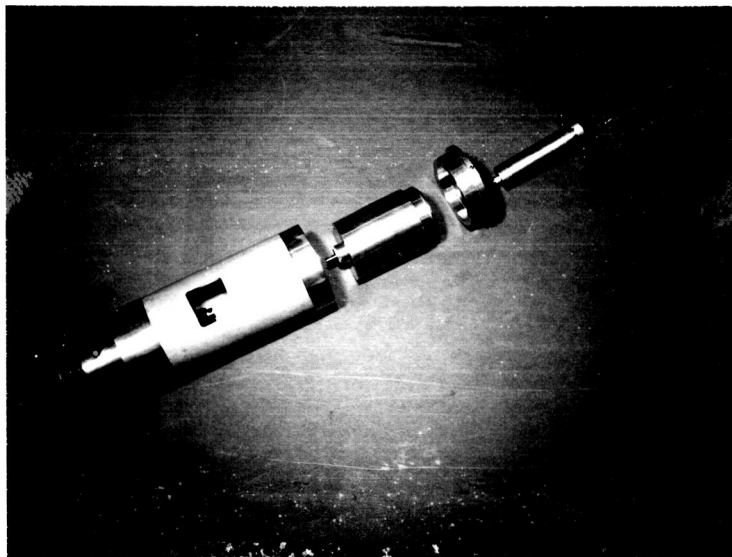
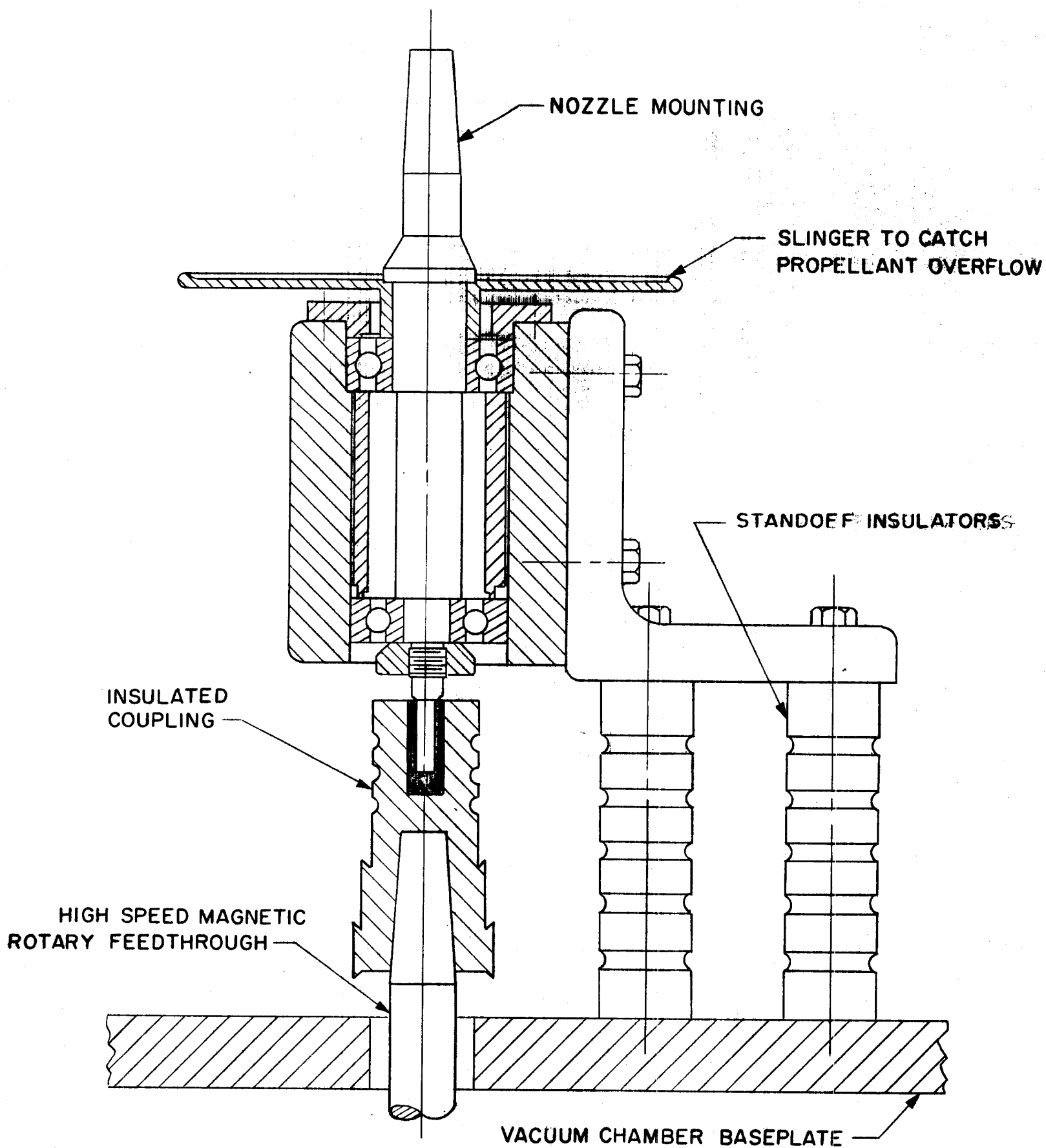


Figure 10. High Speed Rotary Feedthrough



NOZZLE SPINDLE

FIGURE 11

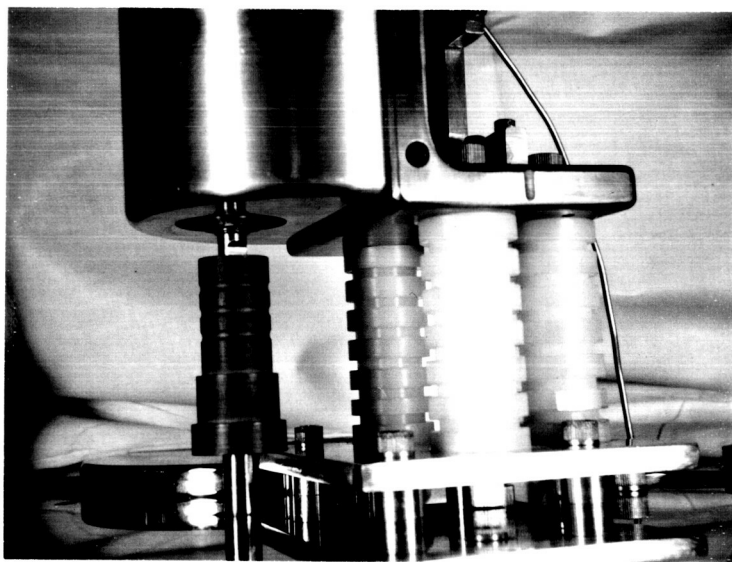
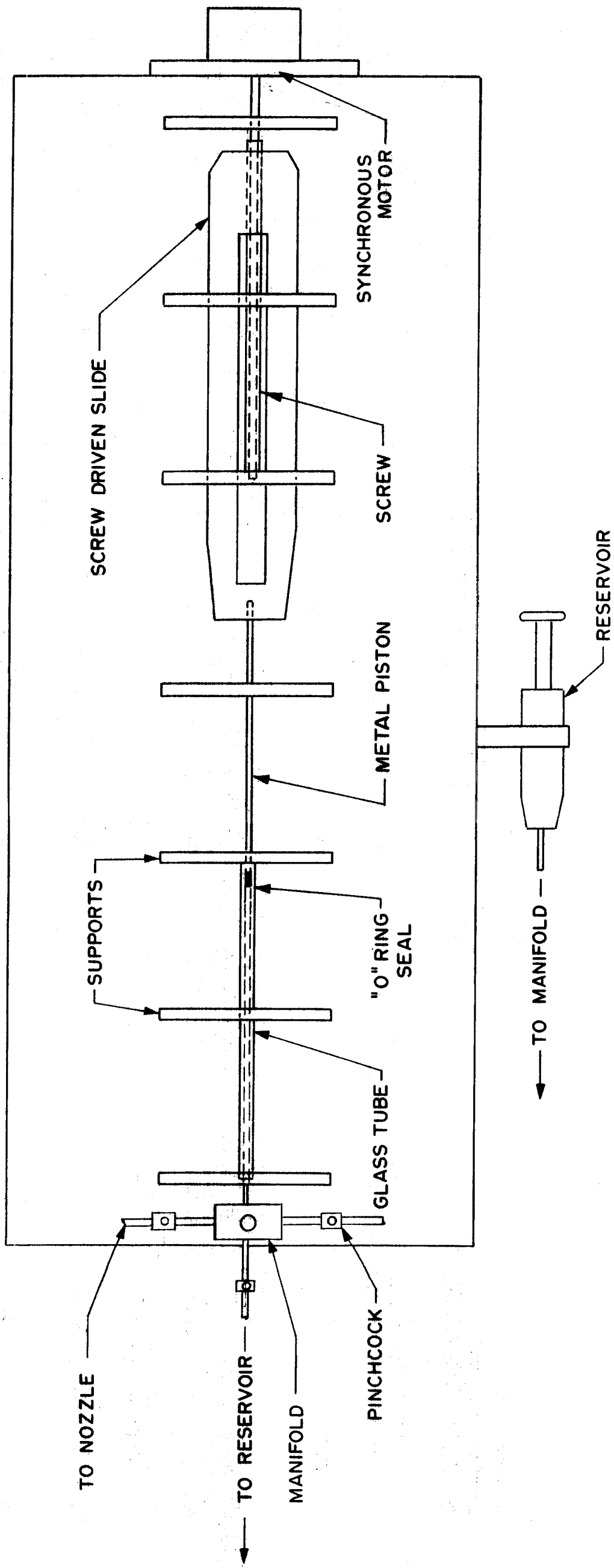


Figure 12. Nozzle Spindle Showing Standoff Insulators and Insulated Coupling



PROPELLANT METERING AND FEED SYSTEM

FIGURE 13

3.1.4 Accelerating System

The geometry of the accelerating system was first studied on an analog consisting of a tightly stretched rubber membrane. The deformation of this membrane simulates the effect of the system components on the electric field and is shown in Figure 14. Small balls were rolled over the analog to study the effect of the field on the focusing of the beam. The balls were given an initial velocity at an angle to the axis to simulate the centrifugal forces.

The accelerating system consists basically of two electrodes as shown in Figure 6: the extractor, a small electrode close to the nozzle to charge and extract the colloids; the collector, a larger electrode a short distance behind the extractor and at the same potential to collect the charged colloids. The position and size of the extractor in relation to the collector affords sufficient shielding of the collector from the electrical field to prevent backstreaming of the collected propellant. Since the nozzle is not located in the center of the vacuum chamber, a cylindrical wire mesh screen at the same potential as the nozzle is used to reestablish axial symmetry and help focus the colloid beam on the collector. The position of the system in the vacuum chamber is shown in Figure 15.

To measure the thrust, an 18° wedge shaped window was machined in the collector. A portion of the beam (one-twentieth) passes through the window and strikes a small circular target which is suspended by a thin wire from an electric micro balance (Reference 12) located in the top of the vacuum chamber (Figure 6). To protect the target from the effect of electrostatic forces, a wire shield surrounds the target and its suspension wire and a wire grid covers the window in the collector (as shown in Figures 16 and 17). The micro balance is protected from the field and the colloids by the large plate in the top of the vacuum chamber as shown in Figure 15. As further protection from the field, a wire mesh shield covers the balance.

3.1.5 High Voltage Connections

The source of high voltage is an electrostatic generator of the pressurized hydrogen insulated constant oblique field type (Reference 12). This generator is capable of producing a variable DC voltage between 0 and 100 kilovolts in either polarity. The main advantage of this type of generator is its low internal capacitance which renders discharges harmless for the operators and reduces considerably the recovery time in case of a discharge occurring inside the vacuum chamber. The system is constructed so that either the nozzle or the accelerating

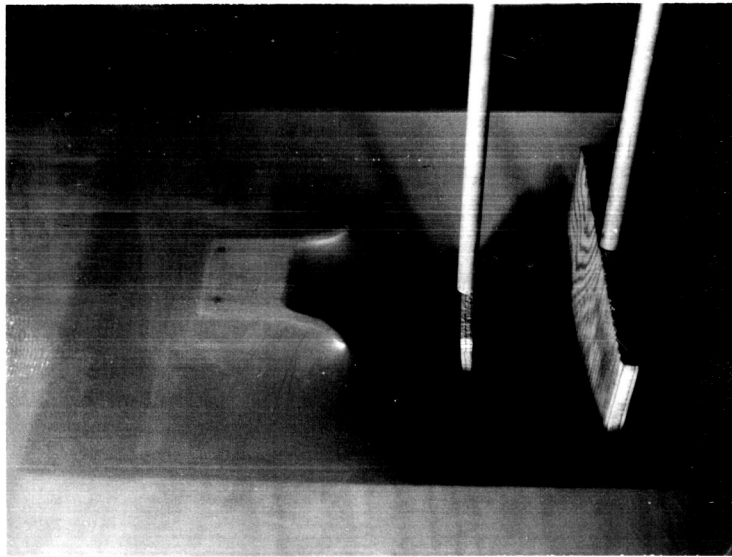


Figure 14. Rubber Analog of Nozzle and Accelerating Electrodes Showing Droplet Trajectory

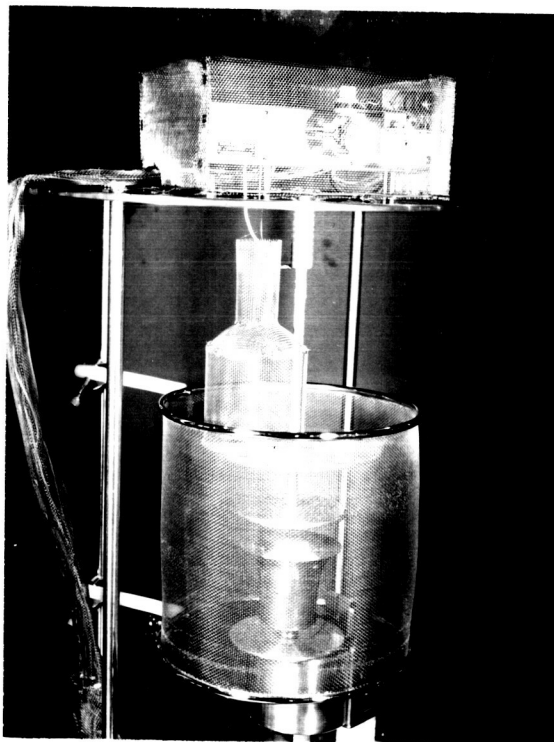


Figure 15. Test Stand with Vacuum Chamber Bell Jar Removed

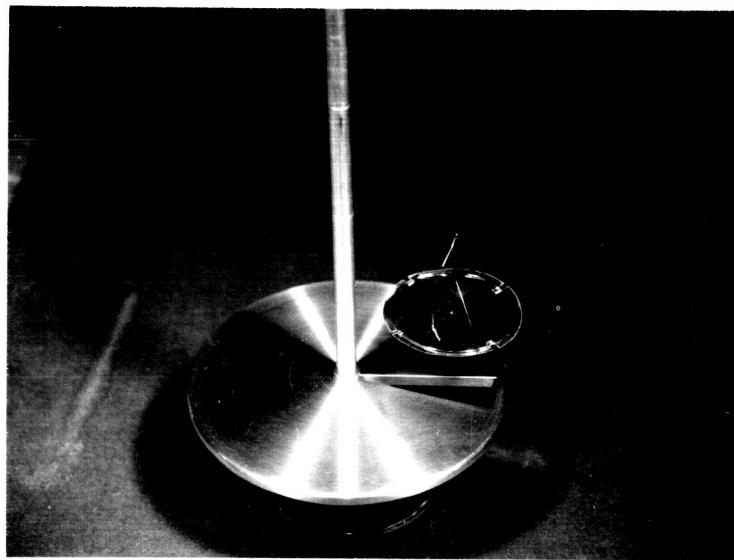


Figure 16. Extractor, Collector, and Target



Figure 17. View of Collector Window Showing Target,
Target Grid and Target Shield

electrodes can be at the high potential. Two high voltage bushings are used; each capable of insulating about 100 kilovolts. The high voltage connection to the nozzle is made by means of the propellant feed tube. The tube passes through the center of one of the high voltage bushings.

3.1.6 Heating System for Operation with Liquid Metals

With this system the propellant feed system, the plumbing, and the nozzle are constantly maintained at a temperature in excess of 150°F. Inside the vacuum chamber two spotlights are aimed at the nozzle and at the propellant supply tube high voltage bushing. The intensity of the lights is regulated by voltage control. The propellant metering and feed system is enclosed in a transparent plastic sheet and all of the connecting tubing to the vacuum chamber is inside a two-inch plastic tube. Hot air from a "heat gun" is circulated inside the plastic envelopes. The temperature of the blower is regulated by voltage control.

3.2 Instrumentation

The measurements to be taken on the system are shown in Figure 18. The arrangement of the instruments is shown in Figure 19. To avoid errors, the quantities to be measured are the subject of several measurements which can be corroborated by additions or subtractions as shown in Figure 18.

3.2.1 Voltage

The output voltage of the electrostatic generator power supply is measured by a voltage-divider type voltmeter. A signal from the voltage divider is fed to an oscillograph for continuous monitoring of the system voltage.

3.2.2 Currents

The nozzle and screen currents are monitored by independent microammeters located on the high voltage bushing of the electrostatic generator. The extractor and collector current is monitored by a single microammeter. The target current is monitored by a galvanometer and a microammeter.

3.2.3 Mass Flow

The total mass flow is determined by the propellant metering and feed system. The various mass flow rates are given

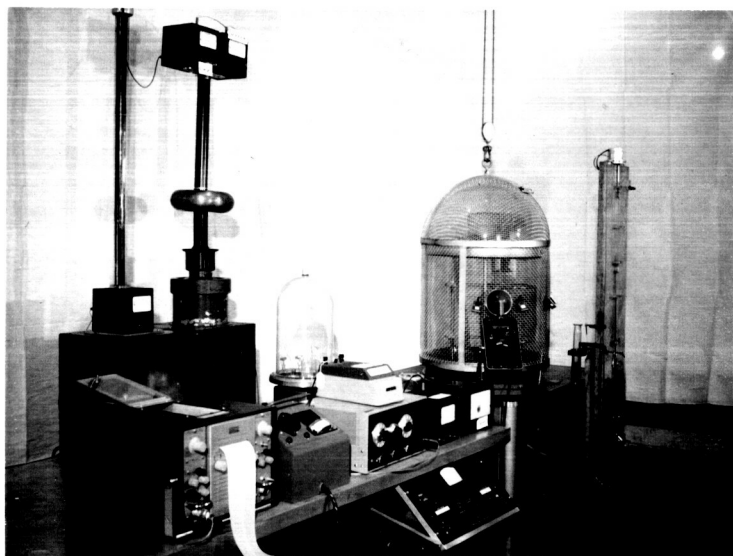


Figure 19. Test Stand with Instrumentation and Auxiliary Equipment

in paragraph 3.1.3 for a density of $1000 \frac{\text{kg}}{\text{m}^3}$. The mass flow of that part of the beam which hits the target is continuously monitored by the micro-balance and is obtained from the oscillograph record.

3.2.4 Thrust

The force on the target is continuously varying due to the accumulation of propellant. The thrust of the beam is measured directly from the micro balance by suddenly turning off the beam. The change in force on the target is the thrust.

3.2.5 Angular Velocity of the Nozzle

The rotating speed of the nozzle is measured with a stroboscopic light. In addition, visual observations of the film flow in the nozzle can be made.

4. SUMMARY AND DISCUSSION OF TEST RESULTS

4.1 Measurements of Propellant Characteristics

Most important factors in the choice of a propellant are its vapor pressure, conductivity, and ability to wet a nozzle material. One is therefore naturally attracted to the oils which are used in high vacuum pumps and among them octoil has so far been found to be the most convenient. As with other commercially available products used as propellant, it contains volatile products which have to be removed by vacuum refluxing. This is accomplished by placing the propellant in a high vacuum and keeping its temperature at about 250°F. Octoil in itself is not conducting (resistivity higher than 10^7 ohms cm) but it can conveniently dissolve up to 5%, by weight, of an organic salt Tetra N Butyl Ammonium Picrate (TNBAP) which introduces ionic conductivity. The values of the resistivity for various concentrations of TNBAP are shown in Figure 20. Octoil wets most materials.

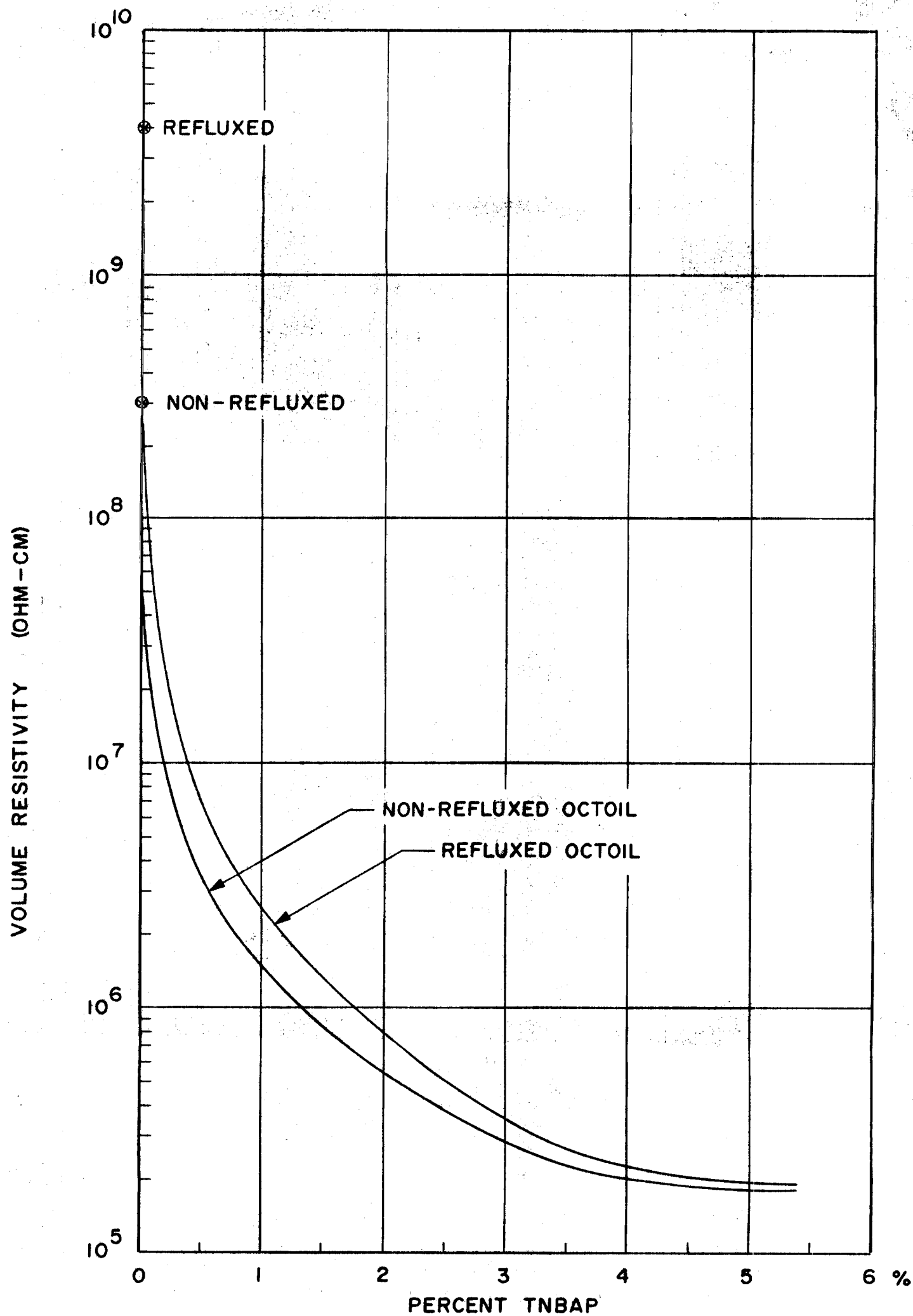
Butyl phthalate, a propellant which has been utilized by C. D. Hendricks at the University of Illinois with some success, has a resistivity of 10^8 ohms cm. It wets most materials.

Glycerol is a liquid with which previous experimenters operating with a needle, have obtained the highest charge-to-mass ratio. Its resistivity was measured with various concentration of two additives --sulphuric acid and antimony trichloride. The results are plotted in Figures 21 and 22 and show that glycerol with these contaminants is capable of a conductivity higher than that of octoil. As we will see later, however, its high vapor pressure makes it an impractical propellant. Furthermore, glycerol wets metals with difficulty and does not wet plastic materials.

Liquid metals are interesting propellants because of their high conductivity and low vapor pressure. The major difficulty of their utilization is that they do not easily wet metallic surfaces. The only surface which has been successfully wetted with liquid metals under this program was a brass nozzle which had been thoroughly cleaned, fluxed, and tinned by dipping. The liquid metal used most extensively in this program is Cerrolow 117.

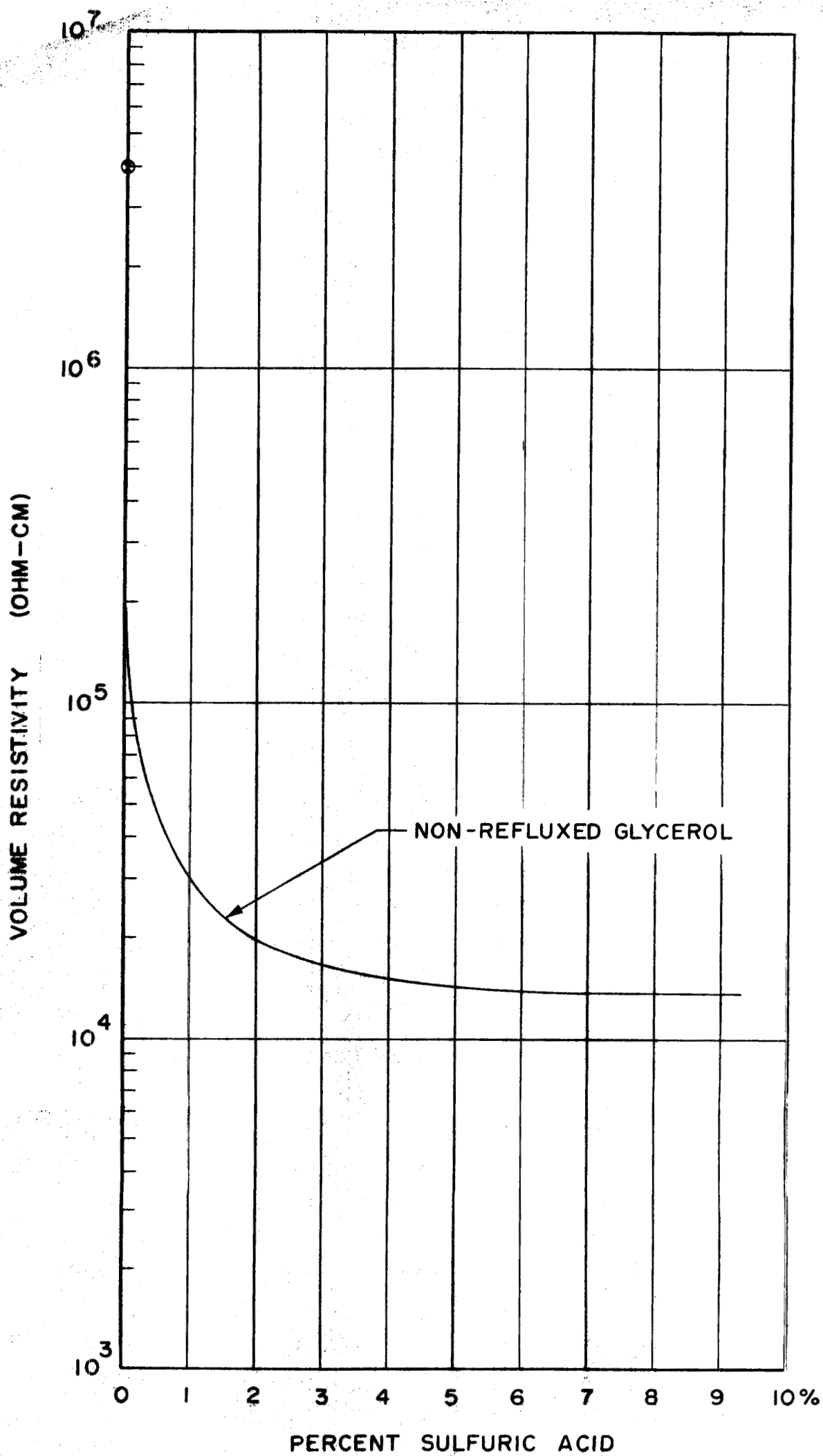
Eutectic mixtures of waxes (Aroclor and Santowax) have been rejected because of their high vapor pressure.

The physical characteristics of the most important propellants are given in Table 2.



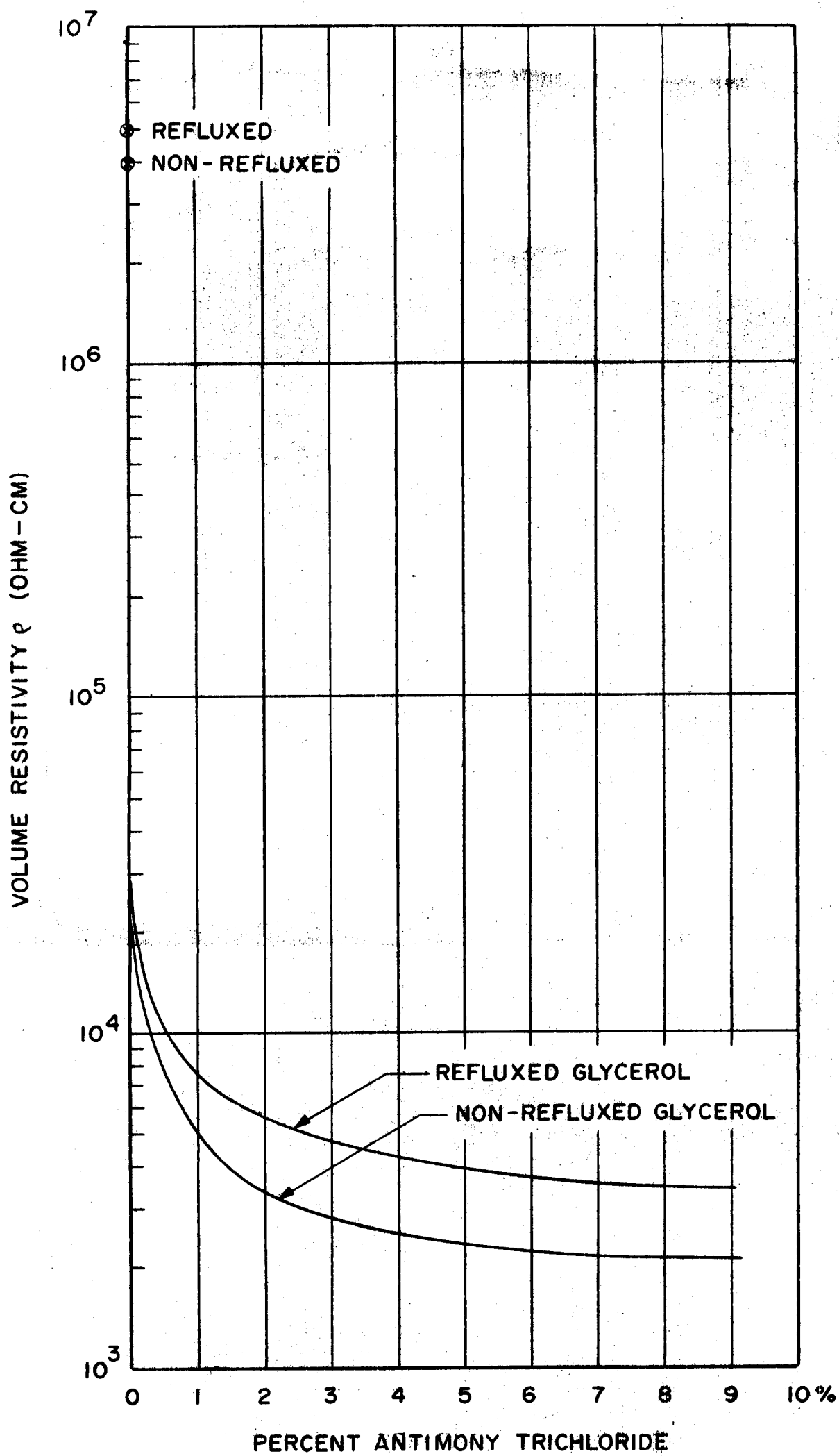
VOLUME RESISTIVITY OF OCTOIL WITH
TETRA N BUTYL AMMONIUM PICRATE

FIGURE 20



VOLUME RESISTIVITY OF GLYCEROL WITH
SULFURIC ACID

FIGURE 21



VOLUME RESISTIVITY OF GLYCEROL WITH
ANTIMONY TRICHLORIDE

FIGURE 22

PROPELLANT	R (OHM-CM)	VAPOR PRESSURE (TORR)	VISCOSITY KG/M - SEC	DENSITY KG/M ³
Octoil	4×10^9	10^{-6}	5.06×10^{-2}	9.83×10^2
Glycerol	5×10^6	10^{-4}	8×10^{-1}	9.98×10^2
Butylphthalate	5×10^9	10^{-5}	1.5×10^{-2}	1.04×10^3
Cerrolow 117 Bu, Pb, Sn, Cd, In	5.18×10^{-5}	$< 10^{-6}$	1.7×10^{-3}	8.86×10^3

TABLE 2. PHYSICAL CHARACTERISTICS OF PROPELLANTS
WITHOUT ADDITIVES.

4.2 Mechanical Tests

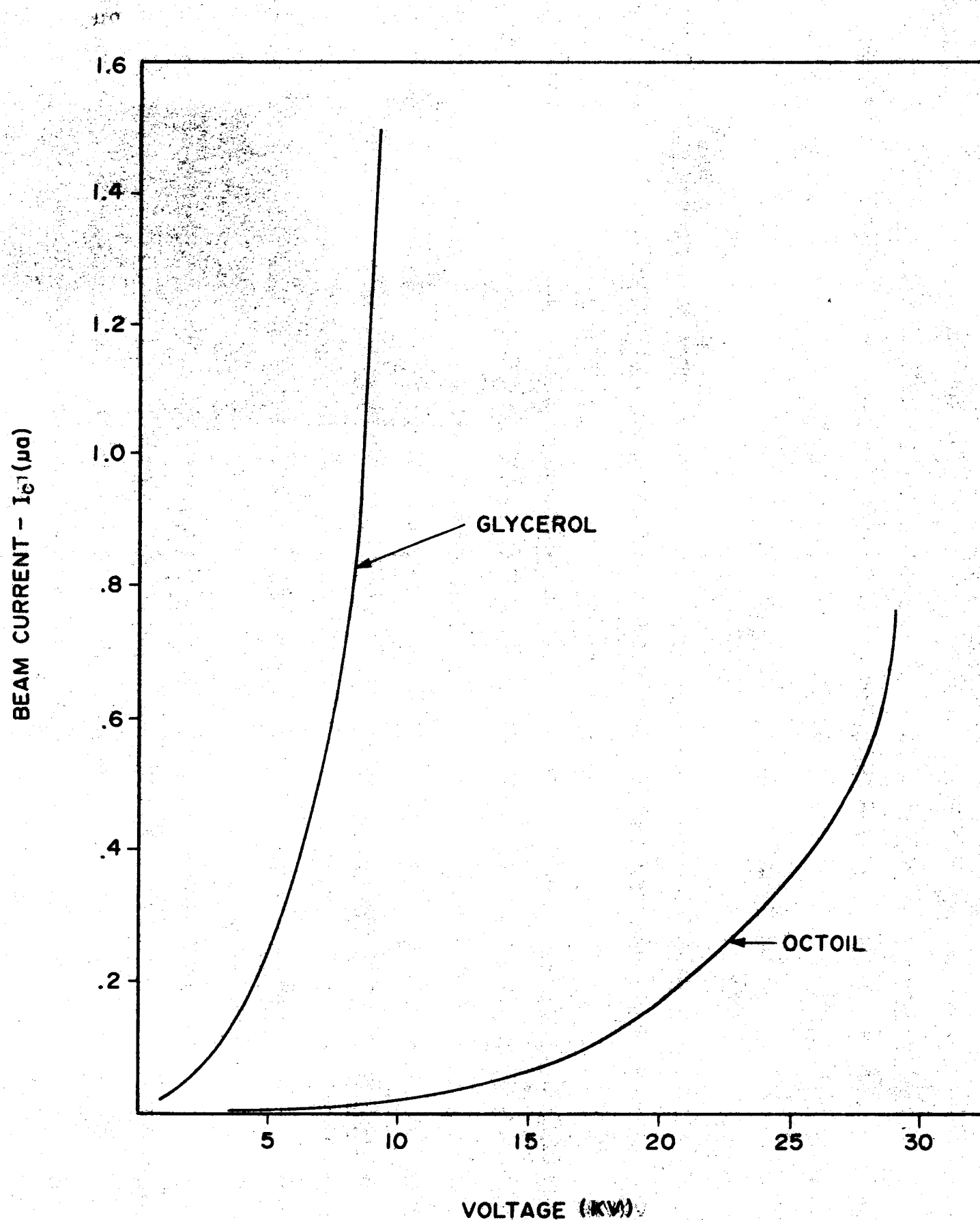
A number of tests were run to determine the proper operation of the propellant delivery system and the behavior of the film flow inside the nozzle. It was found relatively easy to obtain a film of octoil, after adequate cleaning and pre-wetting of the nozzle with octoil. Wet-ting of the nozzle by glycerol was only sufficient to cover three-quarters of the nozzle circumference. As these experiments were carried out with an aluminum nozzle, they required cleaning of the inside of the nozzle with emery paper before each operation. It was never possible to establish a film in the insulating cup with glycerol.

With liquid metal and the aluminum nozzle, the flow was quite discontinuous; the periodic (approximately every five seconds) ejection of a slug of propellant created strong vibrations of the system. Smooth operation was obtained with the brass nozzle which was pre-wetted with liquid metal. However, a uniform film was not obtained.

4.3 Tests with Nozzle at Ground Potential

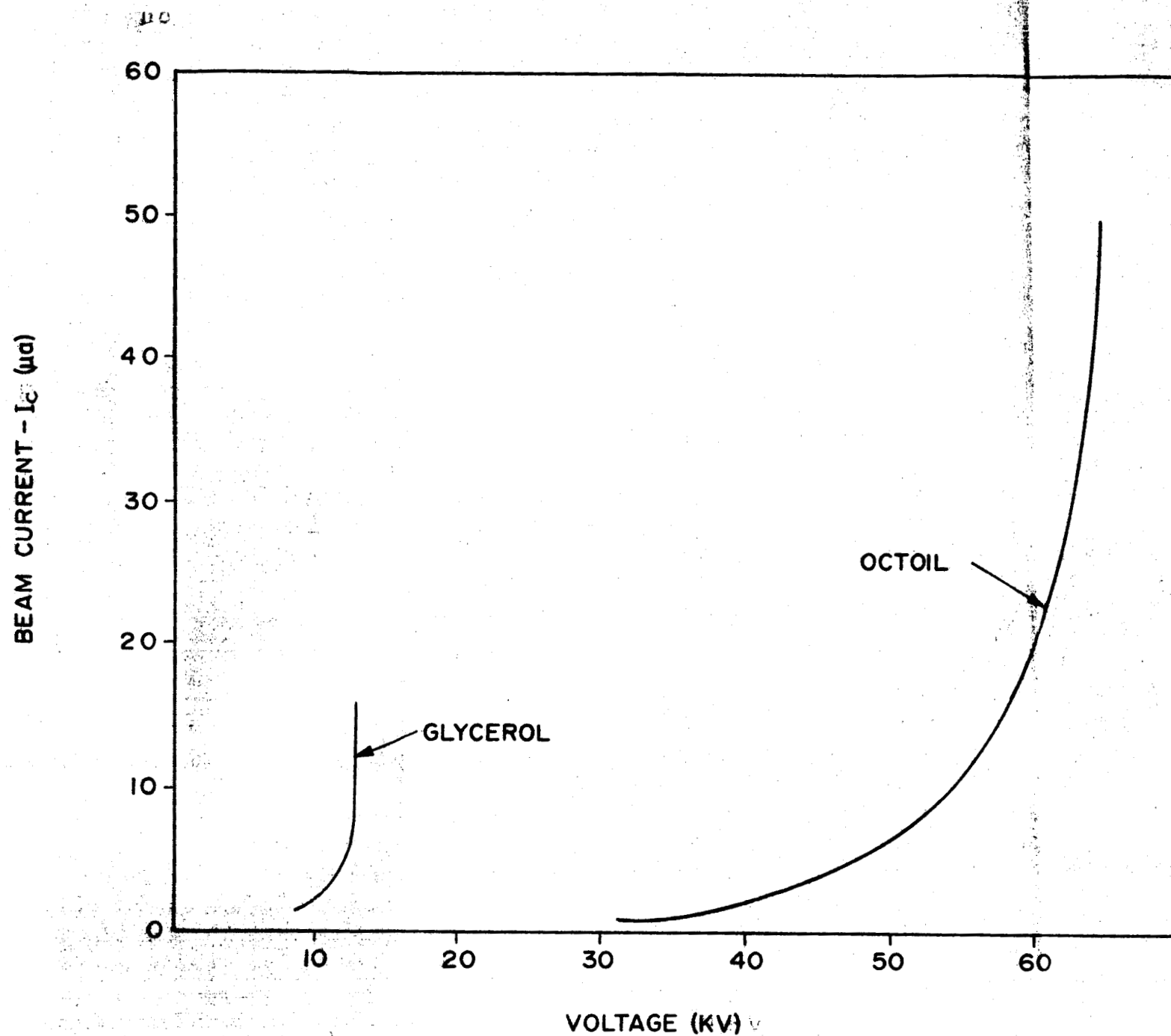
In these tests, the nozzle is mounted on an insulated shaft to permit measurement of the nozzle current. The extractor and collector are at a high negative potential and the screen is at ground potential. With this system, it was possible to attain accelerating voltages of 65 kilovolts, i.e., 50% higher than in the test with the nozzle at the high voltage as described below. However, it was not possible to obtain reliable thrust measurements. An insulated suspension wire had to be used between the microbalance and target and it was not possible to adequately shield this wire from the electrostatic forces.

The beam current as a function of voltage for octoil, glycerol and liquid metal are shown on Figures 23, 24, and 25. Figure 23 shows that charging of the beam occurs even for very low values of the accelerating voltage. Figure 24 shows for the same test the values of the beam currents for higher voltages. At extremal values of the accelerating voltage, the beam current rises sharply and the curve becomes almost vertical at about 60 kilovolts for octoil and 12 kilovolts for glycerol. Above these values of the voltage, breakdown occurs. It then becomes impossible to maintain the high voltage with the electrostatic generator which has a maximum current capability of 300 microamperes. Some tests were run with a high voltage power supply having a high current capability. In this case, beam currents as high as 5 milliamperes have been experienced with glycerol. It appears reasonable to assume therefore that above the values at which the curve ends on Figure 24, the beam charging is due to ionization in the medium which exists around the edge of the nozzle.



BEAM CURRENT AS A FUNCTION OF ACCELERATING
VOLTAGE (LOW VOLTAGE RANGE) INSULATING CUP
MASS FLOW = 1.5×10^{-6} KG/SEC

FIGURE 23



BEAM CURRENT AS A FUNCTION OF ACCELERATING
VOLTAGE (HIGH VOLTAGE RANGE) INSULATING CUP.
MASS FLOW = 1.5×10^{-6} KG/SEC.

FIGURE 24

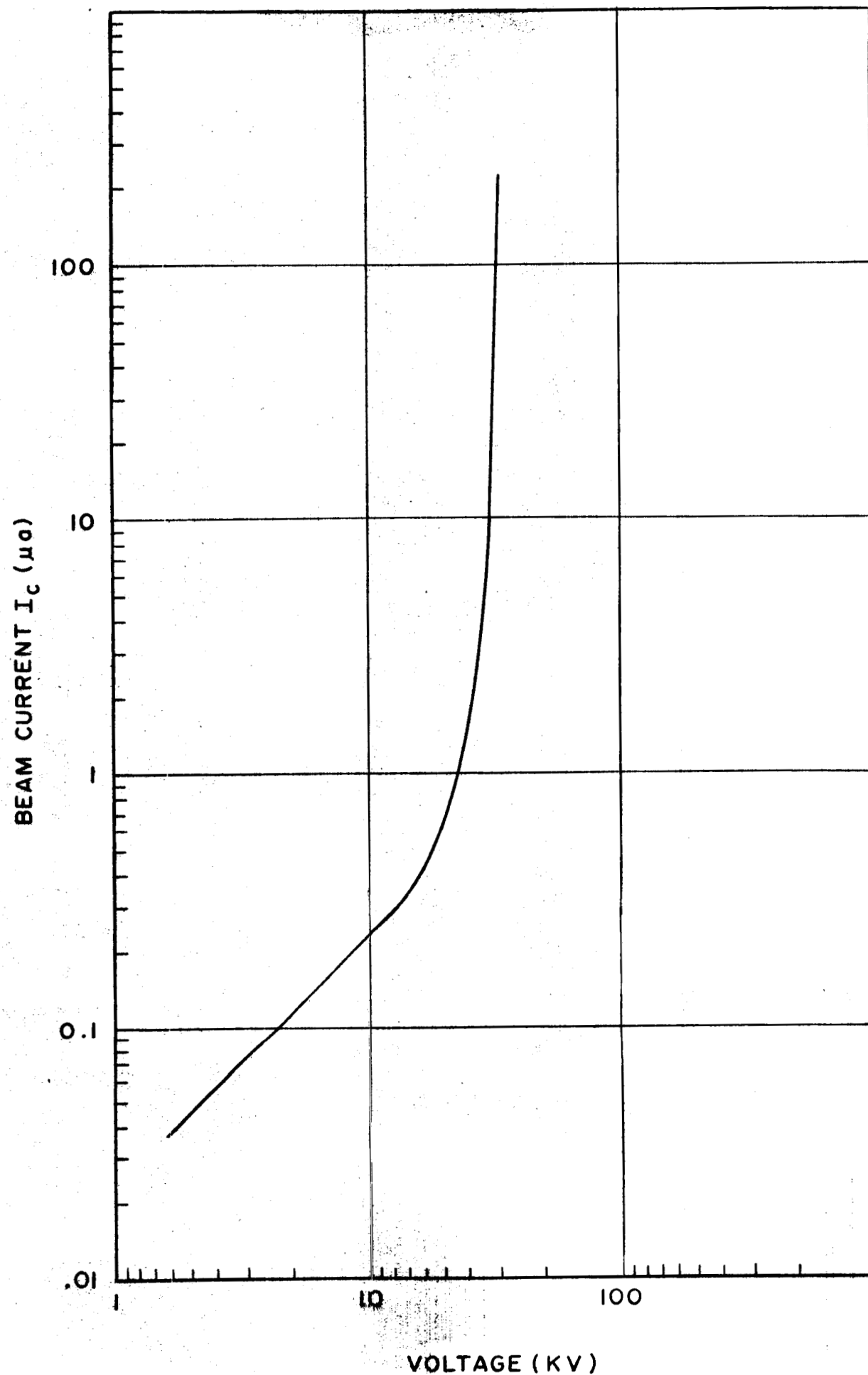
Figure 25 shows an analogous behavior of the beam current during operation with a liquid metal. Proper focusing of the liquid metal beam was difficult to obtain as shown in Figure 26. A portion of the beam has hit the extractor.

It had been suggested that the propellant might evaporate in flight. To prove or disprove this hypothesis, the collector electrode was covered with a sheet of aluminum foil which was weighed before and after the utilization by the system of a known mass of propellant. For octoil, it was concluded that no evaporation took place in flight. For glycerol, approximately 10% of the propellant evaporated.

4.4 Tests with Nozzle at High Voltage

With the collector and extractor at ground potential and the nozzle at a high positive potential, it is possible to completely shield the target and suspension wire from the effect of electrostatic forces. This arrangement has, however, the disadvantage that a voltage on the nozzle higher than 40 kilovolts can only be insulated with great difficulties and the maximum voltage ever attained was 50 kilovolts. These limitations are due primarily to the fact that the nozzle and the screen have to be at the same potential and discharges occur between the screen and the wall of the vacuum chamber. In these experiments, due to the lower operating voltage, it was not possible to obtain values of the ratio of beam current to beam mass flow as high as with the nozzle at ground potential. However, relatively reliable and repeatable test data were obtained which included thrust measurements and therefore made possible calculations of the efficiency. These tests were very useful in providing an understanding of the induction charging mechanism.

The results with octoil are plotted in Figures 27, 28, and 29 for three different mass flows. The points corresponding to the various values of the thrust and the current appear to be located on a straight line. If we now compare this data with the one plotted on Figures 23 and 24, we realize that the straight line appearance is due to the fact that this data pertains to a fairly narrow range of voltage. The top of Figure 27 shows the mass flow on the target corresponding to each test point as determined from electro balance readings. The wide variations of the mass flow is due to instability either in the beam or in the flow inside the nozzle. These variations are less pronounced on Figure 28 in which the mass flow is five times greater, and on Figure 29 in which the mass flow is 20 times as great as that on Figure 21. On Figure 30, the mass flow on the target (see Figure 18) is constant, and is slightly less than one-twentieth the total mass flow indicating a slight lack of symmetry in the beam.

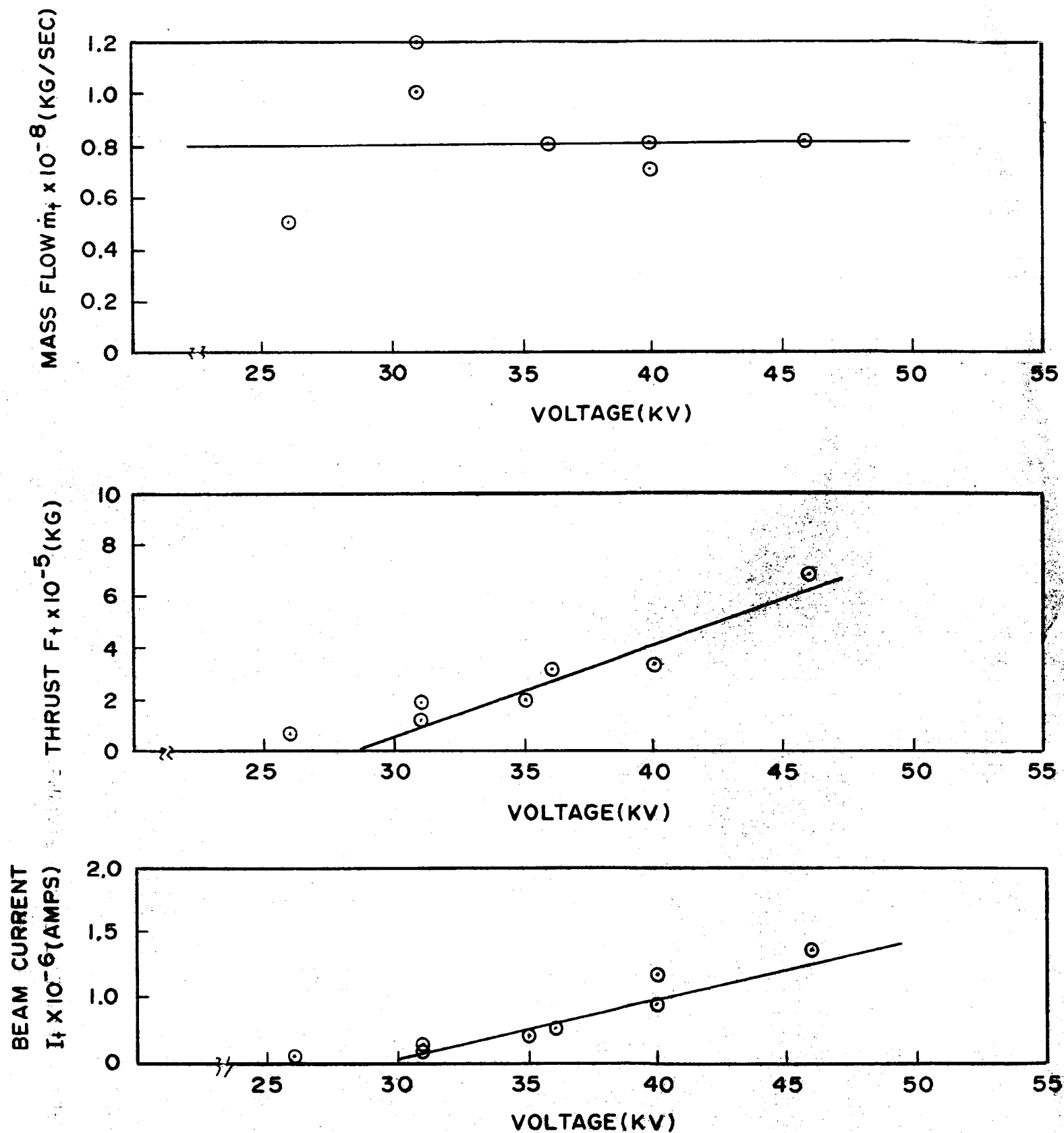


BEAM CURRENT AS A FUNCTION OF ACCELERATING
VOLTAGE WITH LIQUID METAL (MASS FLOW 6.6×10^{-5} KG/SEC)

FIGURE 25

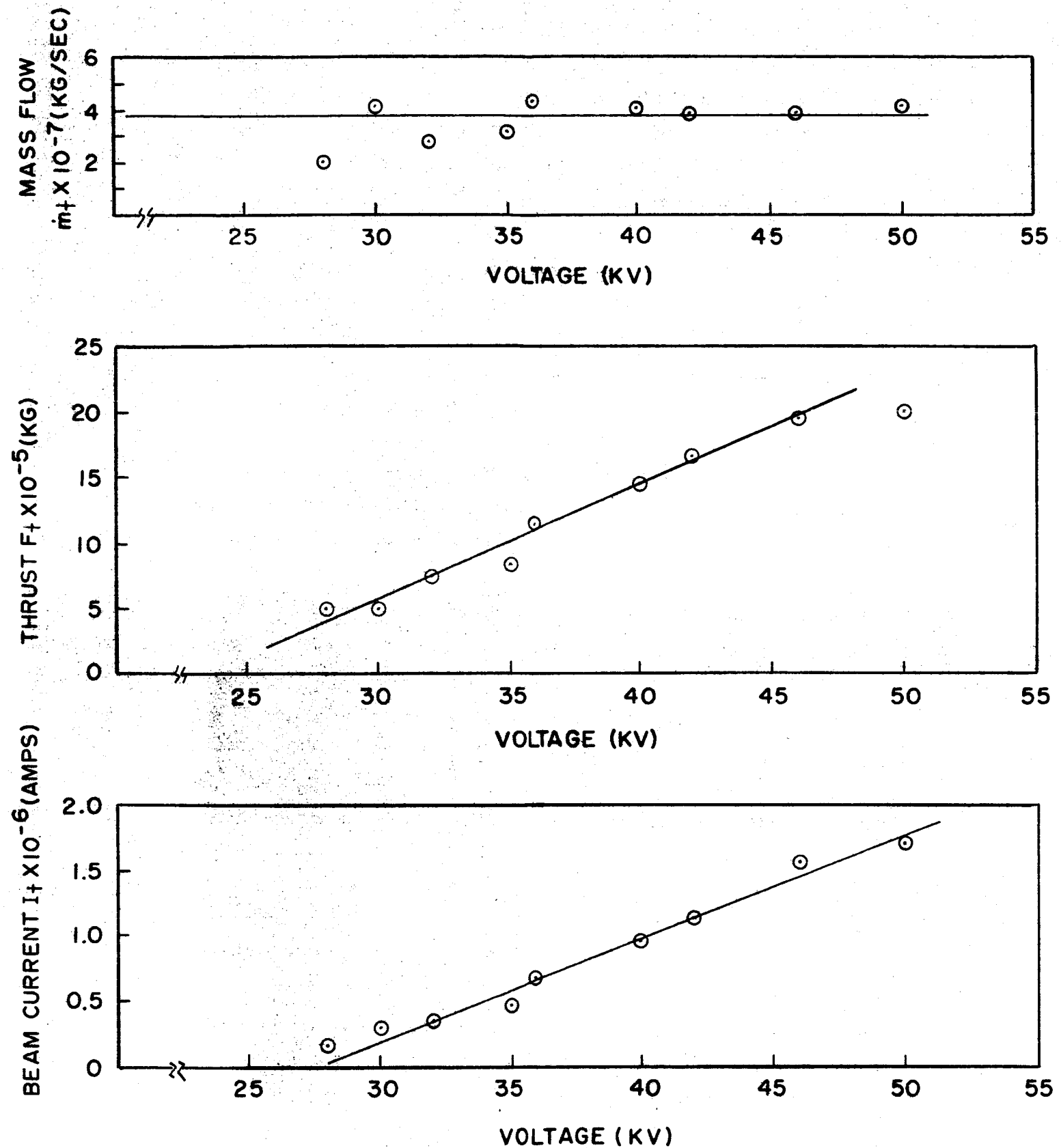


Figure 26. Extractor and Collector with Trace of Liquid Metal Beam



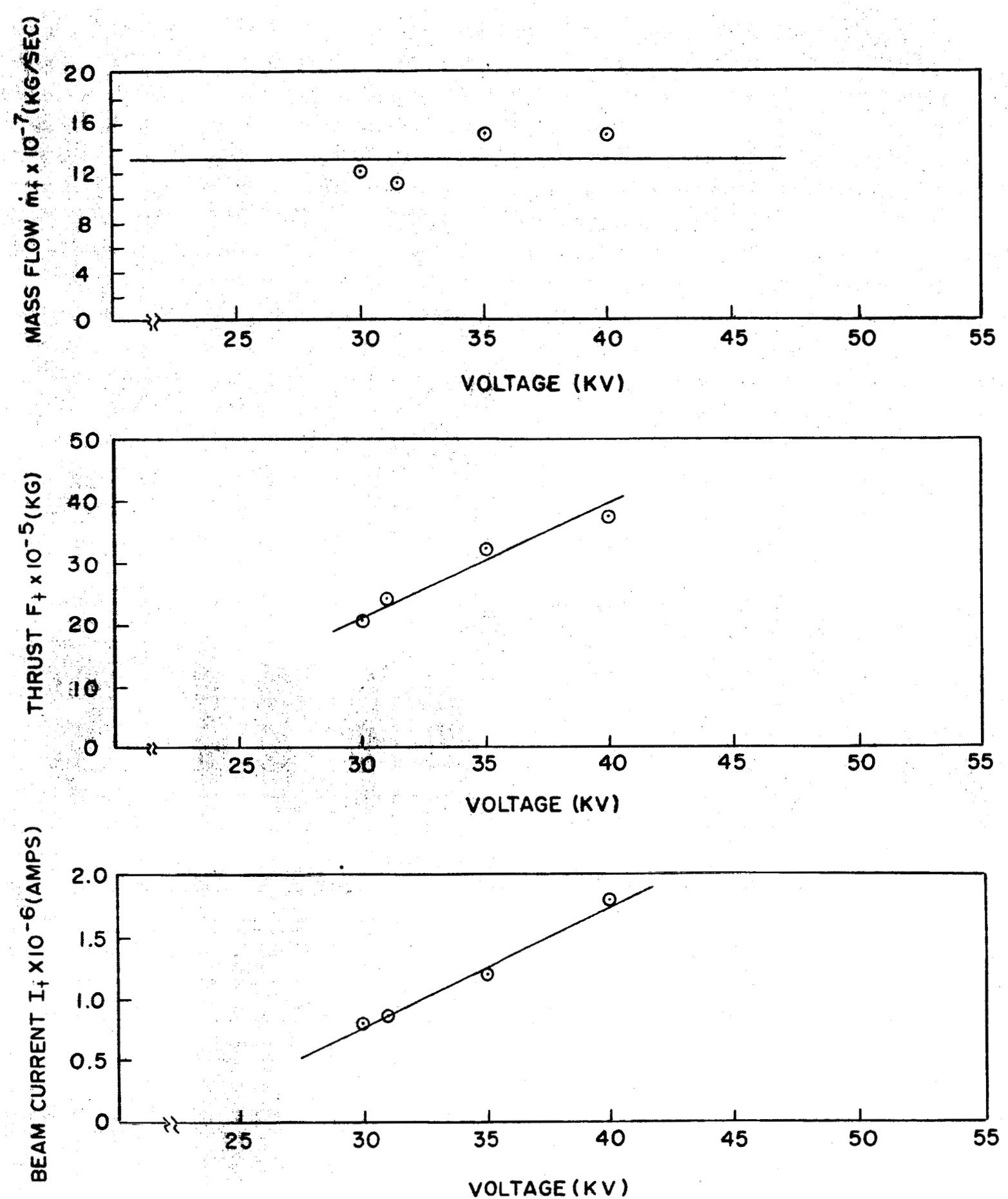
TARGET MASS FLOW, THRUST AND CURRENT
 TOTAL MASS FLOW 1.5×10^{-6} KG/SEC, OCTOIL
 (AVERAGE TARGET MASS FLOW 8.0×10^{-8} KG/SEC)

FIGURE 27



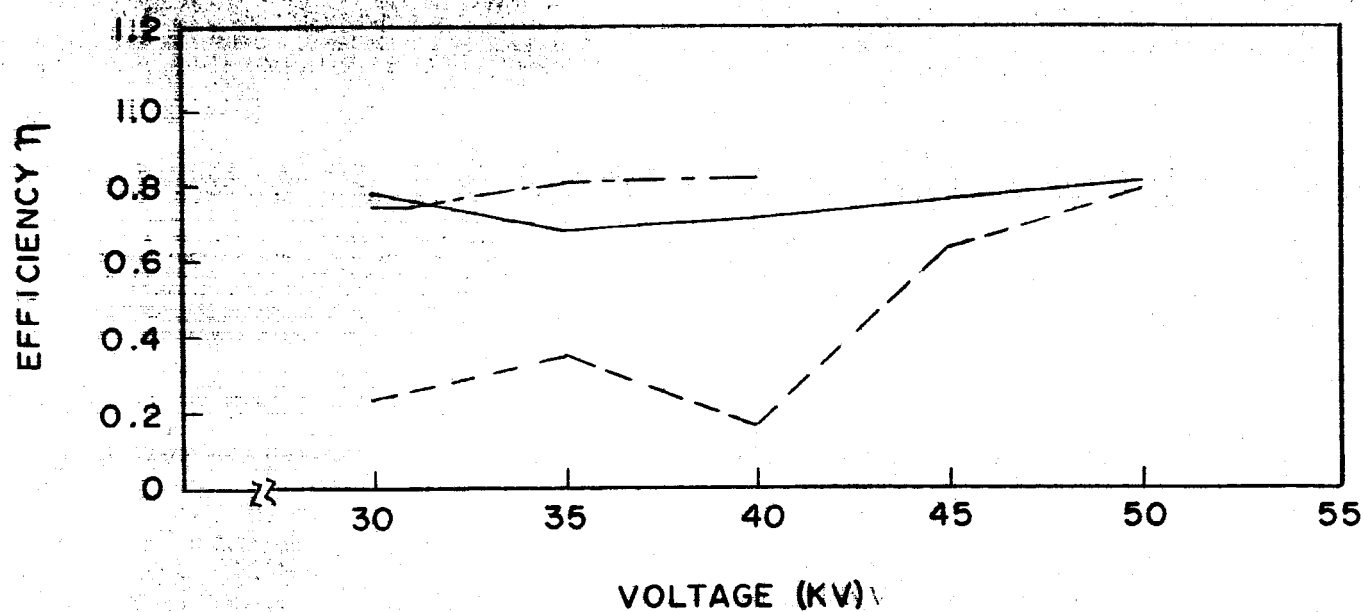
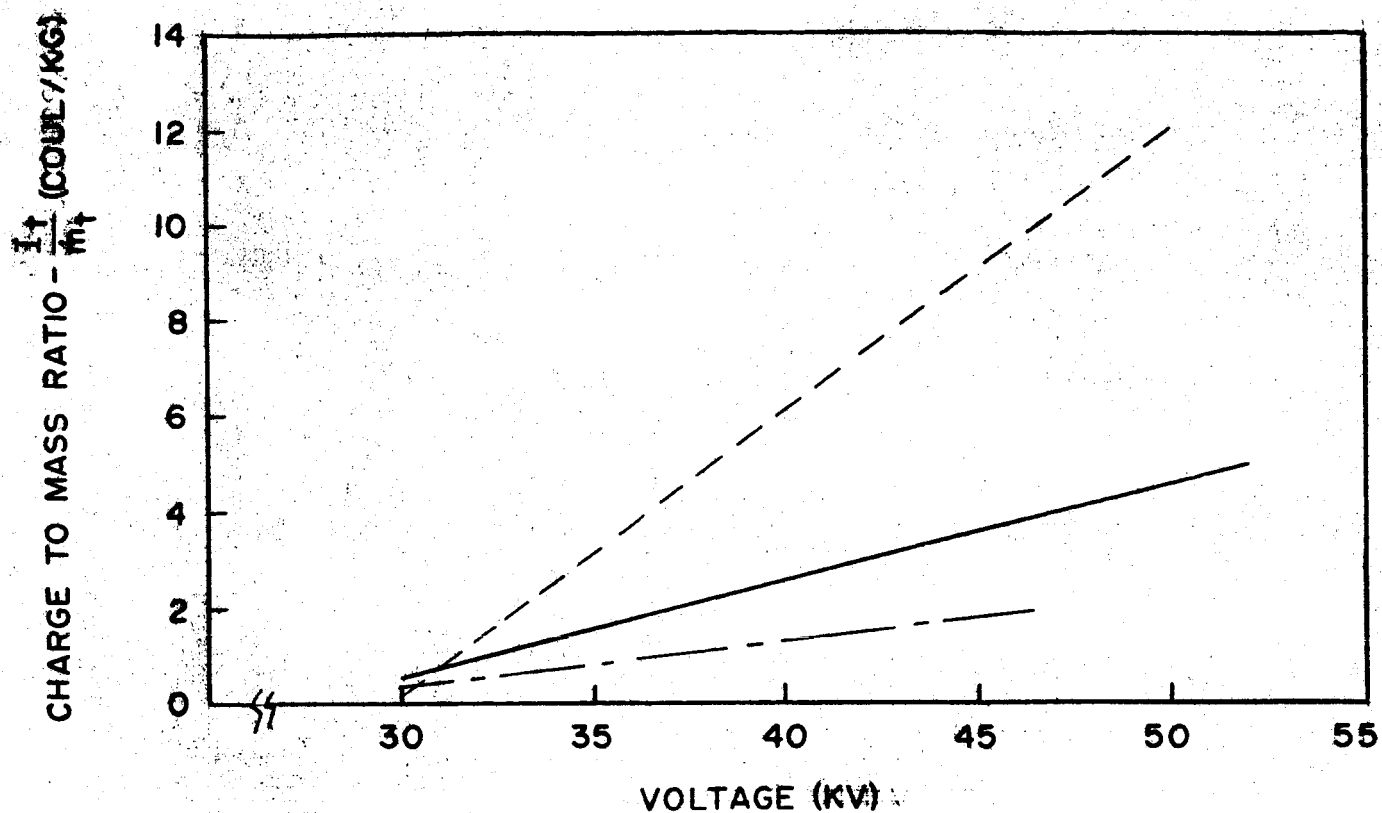
TARGET MASS FLOW, THRUST AND CURRENT AS A FUNCTION OF ACCELERATING VOLTAGE-TOTAL MASS FLOW 7.5×10^{-6} KG/SEC, OCTOIL (AVERAGE TARGET MASS FLOW 3.8×10^{-7} KG/SEC)

FIGURE 28



TARGET MASS FLOW, THRUST AND CURRENT AS A FUNCTION OF
ACCELERATING VOLTAGE - TOTAL MASS FLOW $3.0 \times 10^{-5} KG/SEC$, OCTOIL
(AVERAGE TARGET MASS FLOW $1.3 \times 10^{-6} KG/SEC$)

FIGURE 29



CHARGE TO MASS RATIO AND EFFICIENCY AS A
FUNCTION OF ACCELERATING VOLTAGE FOR
VARIOUS TARGET MASS FLOW RATES.
PROPELLANT - OCTOIL + TNBAP

FIGURE 30

The values of the efficiency corresponding to the data of Figures 27, 28, and 29 exhibit fairly large variations. This is not surprising since the relative error in the efficiency may be as much as five times the relative error in the measured quantities F , I , \dot{m} , and V . A more reliable value of the efficiency is obtained by the following procedure. Straight lines are fitted through the data of Figures 27, 28, and 29. The efficiency is then calculated by using, for each value of V , the values of F , \dot{m} , and I which correspond to the "best fit" curves which have been drawn. In Figure 30, variations of the ratio of beam current to mass flow are shown on the top. For the higher values of the voltage, the efficiency is higher than 75%.

4.5 Comparison Between Predicted and Measured System Performance

The variation of system behavior with controllable experimental elements (i.e., geometry, propellant, \dot{m} , ω , V) was predicted in Section 2.5 above. For reasons described earlier in this Section, the only systematic data against which these predictions can be compared involve the variations of thrust and beam current with variations in voltage and mass flow. We recall from Section 2.5 that for weak space-charge effects

$$I \sim \dot{m}^{+2/3} V$$

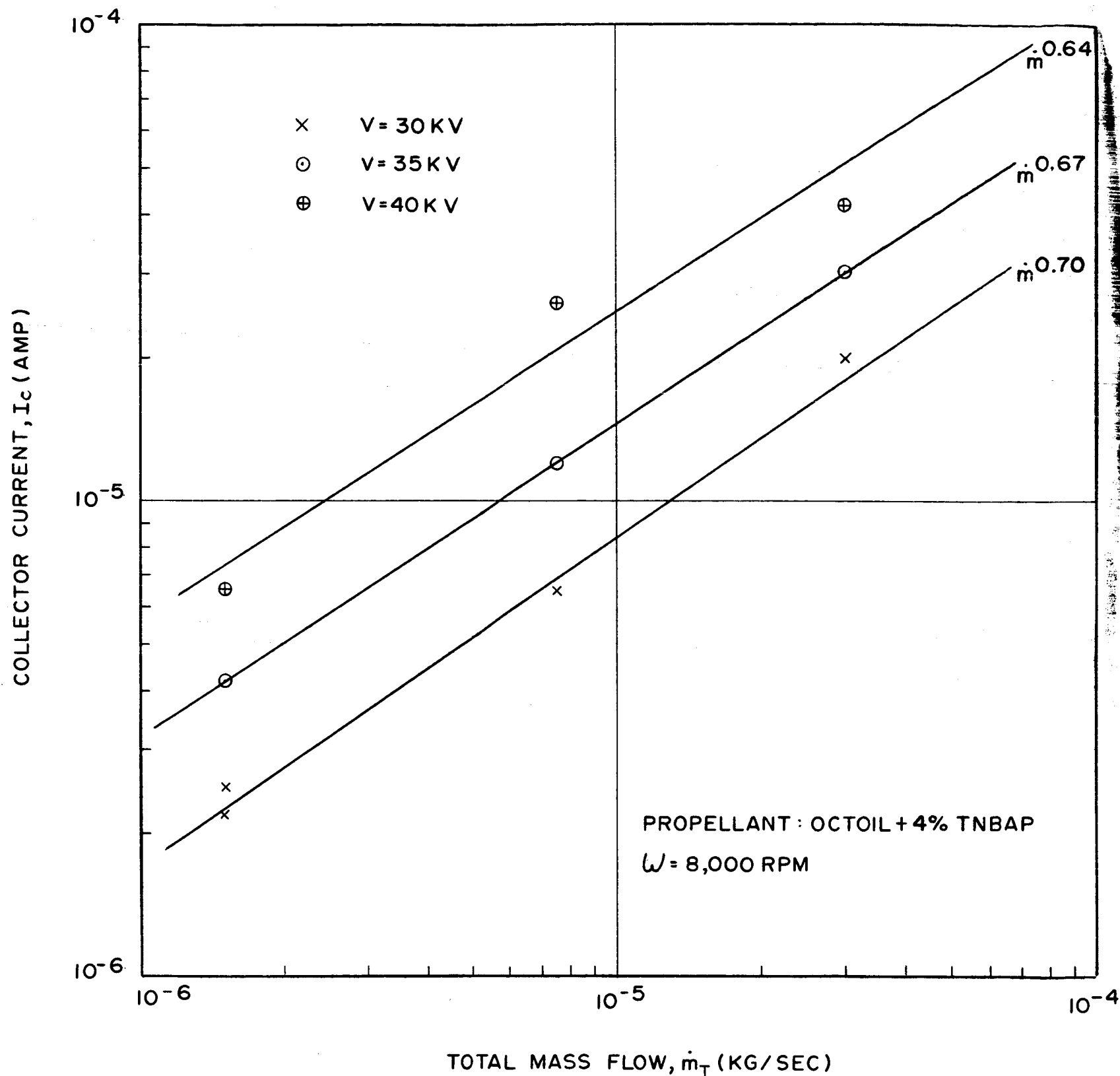
$$F \sim \dot{m}^{+5/6} V$$

whereas for strong space-charge effects

$$I \sim \dot{m}^{-1/3} V^3$$

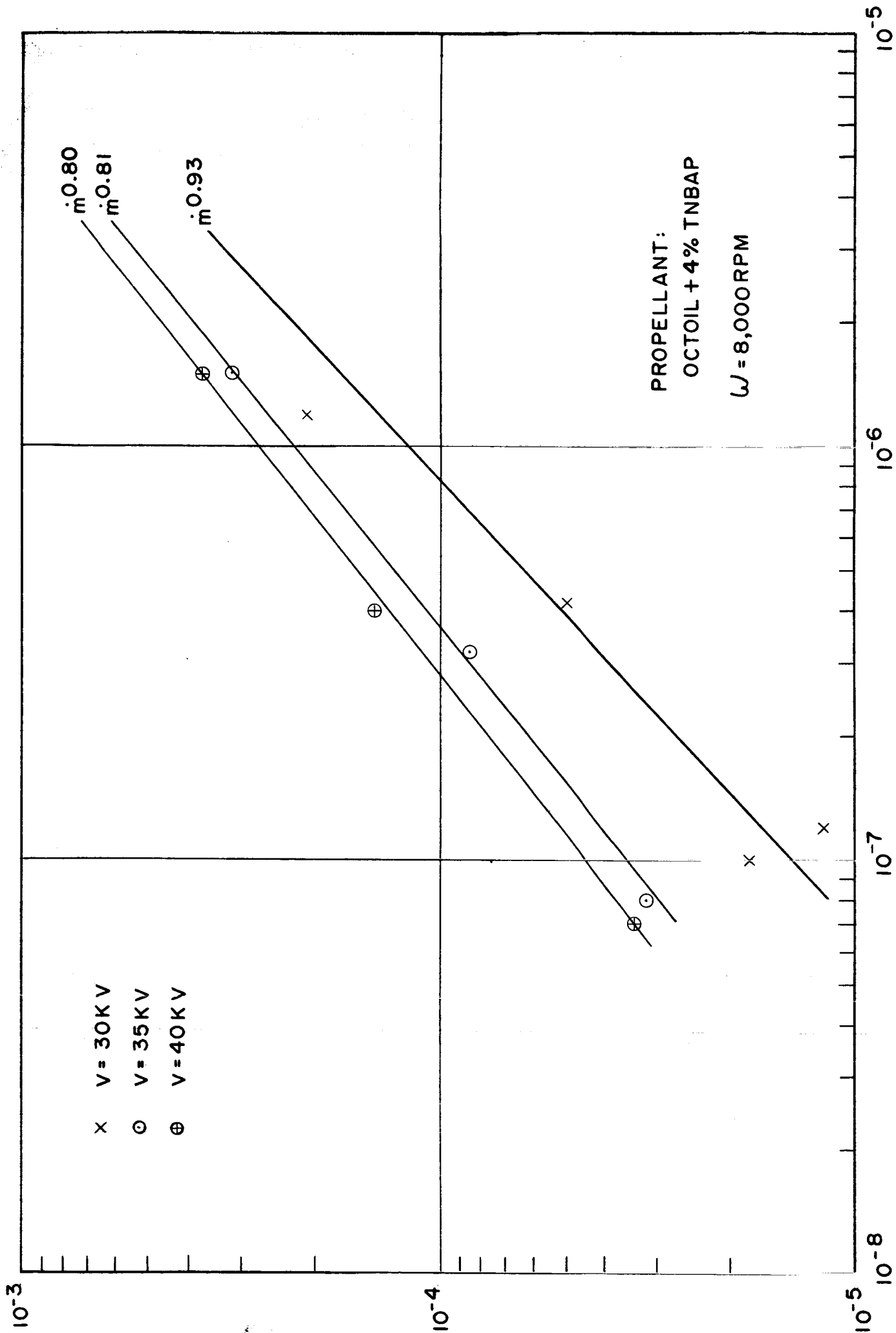
$$F \sim \dot{m}^{+1/3} V^2$$

Since, as indicated earlier, systematic data is available for only one octave of voltages (25 to 50 kv, roughly), it is difficult to infer which, if either, of these power-law dependencies upon voltage is satisfied; a linear variation is, however, a tenable conclusion. The dependence upon mass flow is more easily determined. Thus Figure 31 is a log-log plot of total beam current versus total mass flow for voltages of 30, 35, and 40 kv; straight lines have been fitted to the data and the associated power law dependencies are indicated on the figure. Inspection of this figure shows excellent agreement between the predicted exponent $2/3$ and the inferred exponents 0.64, 0.67, and 0.70. Similarly, Figure 32 is a log-log plot of target thrust versus target mass flow for the same 3 voltages; proceeding as before, we derive from the data exponents 0.80, 0.81, 0.93 to



COLLECTOR CURRENT, I_c , VS TOTAL MASS FLOW, \dot{m}_T , FOR THREE CONSTANT VOLTAGES

FIGURE 31



TARGET MASS FLOW, \dot{m}_t (KG/SEC)

TARGET THRUST, F_t , VS TARGET MASS FLOW, \dot{m}_t , FOR THREE CONSTANT VOLTAGES

FIGURE 32

5. CONCLUSIONS

The general objective of the program was to build and operate a charged colloid generating system using a rotating conical nozzle. A particular objective was the production of particles having a small distribution of charge-to-mass ratio centered in the range of 100 to 1,000 coulombs per kilogram.

The rotating nozzle and accelerator which have been built operate satisfactorily. The associated instrumentation is sufficient to provide test data which can be analyzed and interpreted. This system has produced high currents, and has operated at a high mass flow, but has not yet produced charged particles having a charge-to-mass ratio in the desired range. The rotating nozzle, as instrumented under this program, has provided a good understanding of the phenomena of induction charging. The propellant, and not the charging system, is responsible for the low charge-to-mass ratio. Under this program, only a limited number of propellants have been tried and none was found to possess the required combination of high conductivity, low vapor pressure and ability to wet the nozzle material.

An analytical description of system performance has been derived and shown to predict accurately the experimental results.

One of the most important results of the study is that efficiencies between 70% and 100% have been obtained consistently. These efficiencies have been obtained with low values of the charge-to-mass ratio and of the accelerating voltage (50 kilovolts), resulting in a low specific impulse.

As a laboratory tool for the evaluation of charged colloid generation, the rotating nozzle with the present instrumentation appears to be the most convenient and accurate of all the induction charging methods which have been proposed.

The results which have already been obtained with the rotating nozzle are encouraging and even in this early stage of development compare, in some respects, with those of ion engines. For instance, a thrust of one millipound has been obtained with organic oils with a single nozzle at a low specific impulse but with a remarkable efficiency and practically zero beam interception.

REFERENCES

1. William R. Mickelsen and Harold R. Kaufman, "Electrostatic Thrustors for Space Propulsion, Present and Future", Paper presented at British Interplanetary Society Symposium on Advanced Propulsion Systems, London, England, October 9, 1963.
2. D. Gignoux, H. F. Anton, H. Einbinder, Cosmic, Inc. Report No. 19, "Nozzle for Colloidal Propulsion Analytical Investigation", Report prepared under Contract NAS4-45, August 1961, Cosmic, Inc., Washington, D. C.
3. Victor E. Krohn, "Glycerol Droplets for Electrostatic Propulsion", Progress in Astronautics and Aeronautics, Vol. 9: Electric Propulsion Development; Academic Press, New York, New York; 1963; pp. 435-440.
4. Victor E. Krohn, "Liquid Metal Droplets for Heavy Particle Propulsion", Progress in Astronautics and Rocketry, Vol. 5: Electrostatic Propulsion; Academic Press, New York, New York; 1961; pp. 73-80.
5. Victor E. Krohn, "Research on the Generation and Acceleration of Submicron-Size Particles", Summary Report Prepared Under Contract No. AF 33(616)-6775 by Space Technology Laboratories, Inc., Canoga Park, California, for the Aeronautical Research Laboratories, AFRD, Wright-Patterson Air Force Base, Ohio, August 1959 - February 1962.
6. C. K. Hinrichs, "An Investigation of a Charged Colloid Propulsion System", Aerojet Report AN-683; final technical report prepared under Contract No. AF 49(638)-656, Project No. 9752, Task No. 37521 by the Aerojet-General Corporation, Azusa, California, for the Air Force Office of Scientific Research, Office of Aerospace Research, United States Air Force, May 1959 - July 1962.
7. C. D. Hendricks, Jr., R. S. Carson, J. J. Hogan and J. M. Schneider, "Photomicrograph of Electrically Sprayed Heavy Particles", AIAA Preprint No. 63051-63; presented at the AIAA Electric Propulsion Conference, Colorado Springs, Colorado, March 11-13, 1963.
8. Douglas M. Jamba and Bernard Hornstein, "Charging and Removal of Surface-Condensed Particles for Colloid Propulsion", AIAA Preprint No. 63053-63; presented at the AIAA Electric Propulsion Conference, Colorado Springs, Colorado, March 11-13, 1963.

9. Robert E. Hunter, ARL Technical Note 60-138, "Theoretical Consideration of Nonuniformly Charged Expellant Beams", October 1960, Aeronautical Research Laboratory, Air Force Research Division.
10. David L. Lockwood, William Mickelson, and Vladimir Hamza, "Analytic Space-Charge Flow and Theoretical Electrostatic Rocket Engine Performance", American Rocket Society Electric Propulsion Conference, March 14-16, 1962.
11. Lord Rayleigh, "The Equilibrium of a Liquid Conducting Mass," Philosophical Magazine 14, 184 (1882).
12. Commercial Literature of the Cahn Instrument Company, 15505 Minnesota Avenue, Paramount, California.
13. Dominique Gignoux, "Constant Oblique Field Electrostatic Generator", ARS Preprint, Presented at the ARS Space Power Systems Conference, Santa Monica, California, September 25-28, 1962.

APPENDIX

SPACE CHARGE FLOW BETWEEN PARALLEL PLANES

In the analysis of steady-state space charge flow of particles with charge-to-mass ratio, q/m , passing between two infinite parallel planes separated by a distance, L , and a potential difference, V , all vector quantities are directed normal to the two planes and all spatially varying quantities depend upon only the distance from the source plane. Consequently, it follows from the general law of charge conservation, i.e.,

$$\text{div } \underline{I} + \frac{\partial \sigma}{\partial t} = 0$$

where

\underline{I} = current density

σ = charge density

t = time

that the current density \underline{I} is constant, i.e., spatially non-varying. (These and subsequent equations embody the conventions that the affix "_" beneath a symbol designates a vector quantity, while that same symbol without the affix designates the magnitude of the vector quantity.) Moreover, since the current is purely conducted by the charged particles, it follows that

$$\underline{I} = \sigma \underline{v}$$

$$\text{i.e., } \sigma = \frac{|q|}{q} \frac{I}{v}$$

where

\underline{v} = particle velocity

q = particle charge

But, since the particles leave the source with zero velocity, conservation of energy guarantees that

$$v = (-2 q \psi / m)^{1/2}$$

where ψ is the potential measured from the source plane.

Thus Poisson's equation for the potential becomes

$$\frac{d^2 \psi}{dx^2} = \frac{-\sigma}{\epsilon_0} = -\frac{|q| J}{q \epsilon_0 V} = \frac{-|q| J}{q \epsilon_0 (-2 q \psi/m)^{1/2}}$$

subject to the boundary conditions

$$\psi(x=0) = 0; \left. \frac{d\psi}{dx} \right|_{x=0} = -\frac{|q|}{q} E_0; \psi(x=L) = V$$

where x = distance measured from the source plane

E_0 = electric field at source plane.

With the potential and distance normalized by V and L , respectively, the problem is specified by the equations

$$\Psi'' = \alpha \Psi^{-1/2}$$

$$\Psi(\xi=0) = 0; \Psi'(\xi=0) = e_0; \Psi(\xi=1) = 1$$

where

$$\Psi \equiv \psi/V = \text{dimensionless potential} > 0$$

$$\xi \equiv x/L = \text{dimensionless distance from source plane}$$

$$\alpha \equiv J/J_n > 0$$

$$J_n \equiv -\frac{qV}{|q|} \epsilon_0 (-2 q V/m)^{1/2} / L^2 = \epsilon_0 (2 |q/m|)^{1/2} |V|^{3/2} / L^2$$

= normalizing current density

$$e_0 \equiv E_0/E_0^* > 0$$

E_0^* = electric field at source plane in vacuum (i.e., where

$$J=0) = -qV/|q|L = |V|/L$$

prime, "", denotes differentiation with respect to ξ . Since the second-order Poisson equation requires only two boundary conditions for

its solution, the presence of the third boundary condition makes it possible to relate the current density, J , and the source field, E_o , and, in particular, to determine the space-charge-limited current density, J^* , i.e., the value of J for which $E_o = 0 = e_o$. (It is clear from the equations presented above that when $J = 0$, $\Psi = \xi$ and therefore $E_o = E_o^* = |V|/L$, i.e., $e_o = 1$.) Thus the approach from this point is to i) impose two of the boundary conditions and thereby determine the solution of Poisson's equation and ii) impose the third boundary condition on this solution and thereby determine both J^* and the relation between e_o and $j \equiv J/J^*$.

The solution of Poisson's equation proceeds as follows.

$$\frac{d}{d\Psi} \left(\frac{\Psi'^2}{2} \right) \equiv \frac{d^2\Psi}{d\xi^2} = \alpha \Psi^{-1/2}$$

$$\frac{\Psi'^2}{2} \bigg|_{e_o}^{\Psi'} = 2 \alpha \Psi^{1/2} \bigg|_0^{\Psi}$$

$$\frac{\Psi'^2}{2} - e_o^2 = 2 \alpha \Psi^{1/2}$$

$$\frac{d\Psi}{d\xi} \equiv \Psi' = \left[e_o^2 + 4 \alpha \Psi^{1/2} \right]^{1/2}$$

$$\xi = \int_0^{\Psi} \frac{dz}{[e_o^2 + 4 \alpha z^{1/2}]^{1/2}}$$

By the substitution $s = z^{1/2}$

$$\xi = \int_0^{\Psi^{1/2}} \frac{2s ds}{[e_o^2 + 4 \alpha s]^2}^{1/2}$$

By integration by parts or, equivalently, by Formula #96 of Peirce's Table of Integrals,

$$\xi = \frac{-(e_o^2 - 2 \alpha s)(e_o^2 + 4 \alpha s)^{1/2}}{6 \alpha^2} \bigg|_0^{\Psi^{1/2}}$$

i.e.,

$$\xi = \frac{e_o^3 - (e_o^2 - 2\alpha \Psi^{1/2})(e_o^2 + 4\alpha \Psi^{1/2})^{1/2}}{6\alpha^2}$$

This is the desired solution of Poisson's equation and is expressed implicitly, i.e., ξ is given as a function of Ψ , rather than vice versa. In deriving this result, we have employed the two boundary conditions: $\Psi(\xi = 0) = 0$ and $\Psi'(\xi = 0) = e_o$.

By applying the third boundary condition, viz., $\Psi(\xi = 1) = 1$, to the solution of Poisson's equation, we obtain the following equation for α :

$$\begin{aligned} 1 &= \frac{e_o^3 - (e_o^2 - 2\alpha)(e_o^2 + 4\alpha)^{1/2}}{6\alpha^2} \\ 6\alpha^2 - e_o^3 &= - (e_o^2 - 2\alpha)(e_o^2 + 4\alpha)^{1/2} \\ 36\alpha^4 - 12\alpha^2 e_o^3 + e_o^6 &= (4\alpha^2 - 4\alpha e_o^2 + e_o^4)(4\alpha + e_o^2) \\ &= 16\alpha^3 - 12\alpha^2 e_o^2 + e_o^6 \\ 36\alpha^4 - 16\alpha^3 + 12\alpha^2 e_o^2(1 - e_o) &= 0 \\ 9\alpha^2 - 4\alpha + 3e_o^2(1 - e_o) &= 0 \\ \alpha^2 - \frac{4}{9}\alpha + \frac{e_o^2}{3}(1 - e_o) &= 0 \\ \alpha = \frac{2}{9} \left[1 \pm \sqrt{1 - \frac{27}{4}e_o^2(1 - e_o)} \right] \end{aligned}$$

For $e_o = 2/3$, the solutions corresponding to the plus and minus signs coincide. For $e_o > 2/3$, the solution corresponding to the minus sign must be used, since we know that for $e_o = 1$, $\alpha = 0$, i.e., $J = 0$. Conversely, for $e_o < 2/3$, the solution corresponding to the plus sign must be used, in order to avoid the physically unacceptable conclusion that $\alpha = 0$ when $e_o = 0$. Thus we conclude that

$$\alpha = \frac{2}{9} \left[1 \pm \sqrt{1 - \frac{27}{4}e_o^2(1 - e_o)} \right] \quad \begin{aligned} 0 \leq e_o &\leq 2/3 \\ 2/3 \leq e_o &\leq 1 \end{aligned}$$

It follows that α is a monotonically decreasing function of e_o and that for space-charge-limited conditions

$$\alpha = \alpha_{\max} = \alpha(e_o = 0) = \frac{4}{9}$$

Thus, we obtain

$$J^* = J_n \left[\alpha(e_o = 0) \right] = \frac{4}{9} J_n = \frac{4}{9} \frac{\epsilon_o (2 |q/m|)^{1/2} |V|^{3/2}}{L^2}$$

Finally, in terms of the normalized current density, j , defined as J/J^* , we obtain

$$\begin{aligned} j \equiv \frac{J}{J^*} &= \frac{J}{(4/9) J_n} = \frac{9}{4} \alpha \\ &= \frac{1}{2} \left[1 \pm \sqrt{1 - \frac{27}{4} e_o^2 (1 - e_o)} \right] \quad \begin{array}{l} 0 \leq e_o \leq 2/3 \\ 2/3 \leq e_o \leq 1 \end{array} \end{aligned}$$

FINAL REPORT DISTRIBUTION LIST

CONTRACT NAS3-2509

<u>Addressee</u>	<u>Number of Copies</u>
1. NASA Headquarters FOB - 10B 600 Independence Avenue, S. W. Washington, D. C. Attention: RNT/James Lazar	2
2. NASA-Lewis Research Center 21000 Brookpark Road Cleveland, Ohio 44135 Attention: J. H. Childs	2
3. NASA-Lewis Research Center 21000 Brookpark Road Cleveland, Ohio 44135 Attention: R. D. Shattuck	7
4. NASA-Lewis Research Center 21000 Brookpark Road Cleveland, Ohio 44135 Attention: Spacecraft Technology Procurement Section John H. DeFord	1
5. NASA-Lewis Research Center 21000 Brookpark Road Cleveland, Ohio 44135 Attention: Technology Utilization Office	1
6. NASA-Lewis Research Center 21000 Brookpark Road Cleveland, Ohio 44135 Attention: Technical Information Division	1
7. Commander Aeronautical Systems Division Wright-Patterson Air Force Base, Ohio Attention: AFAPL (APIE)/Mr. Robert Supp	1
8. NASA-Lewis Research Center 21000 Brookpark Road Cleveland, Ohio 44135 Attention: Library	2

<u>Addressee</u>	<u>Number of Copies</u>
9. NASA-Lewis Research Center 21000 Brookpark Road Cleveland, Ohio 44135 Attention: C. T. Norgren	2
10. NASA-Marshall Space Flight Center Huntsville, Alabama Attention: (M-RP-DIR)/E. Stuhlinger	1
11. NASA Scientific and Technical Information Facility Box 5700 Bethesda 14, Maryland Attention: RQT-2448/NASA Representative *Plus a Reproducible	6*
12. Rocketdyne Division of North American Aviation, Inc. Electric Propulsion Section Canoga Park, California Attention: Dr. J. F. Hon	1
13. Rocket Power, Inc. 3016 East Foothill Boulevard Pasadena, California Attention: Dr. S. Singer	1
14. Ion Physics Corporation Burlington, Massachusetts Attention: Dr. Sam Nablo	1
15. Astrosystems, Inc. 82 Naylor Avenue Livingston, New Jersey Attention: Mr. R. E. Wiech, Jr.	1
16. Space Technology Laboratories, Inc. Physical Research Laboratories 8433 Fallbrook Avenue Canoga Park, California Attention: Dr. D. B. Langmuir	1
17. Reaction Motors Division Thiokol Chemical Corporation Denville, New Jersey Attention: Dr. Wilby Courtney	1

<u>Addressee</u>	<u>Number of Copies</u>
18. Aerojet-General Nucleonics P. O. Box 77 San Ramon, California Attention: Dr. John Luce	1
19. Gruman Aircraft Engineering Corporation Bethpage, Long Island New York Attention: Mr. Paul Grinoch	1
20. Hughes Research Laboratories 3011 Malibu Canyon Road Malibu, California Attention: Dr. Ron Knechtli	
21. Electro-Optical Systems, Inc. 300 North Halstead Street Pasadena, California Attention: Dr. A. T. Forrester	1
22. The Martin Company P. O. Box 5837 Orlando, Florida 32808 Attention: Engineering Library MP 30	1
23. AFWL Kirtland Air Force Base, New Mexico Attention: WLPC/Capt. C. F. Ellis	1
24. Aerospace Corporation P. O. Box 95085 Los Angeles, California 90045 Attention: Library Technical Documents Group	1
25. Westinghouse Astronuclear Labs. Pittsburgh, Pennsylvania 15234 Attention: H. W. Szymanowski, Mgr. Electrical Propulsion Lab.	1

ABSTRACT

A method for obtaining induction-charged colloids has been developed which consists in expending a thin film of liquid inside a rapidly spinning nozzle and pulling off the film at the edge of the nozzle by an intense electric field. Measurements have been made of beam current, mass flow, thrust and efficiency. A theoretical study of induction-charged colloids in general has resulted in the establishment of a model which includes the space-charge effects. Advantages of the spinning nozzle method for low specific impulse electric thrusters are discussed.